Seismic monitoring of the STIMTEC hydraulic stimulation experiment in anisotropic metamorphic gneiss

Carolin M. Boese[1], Grzegorz Kwiatek[1], Thomas Fischer[2], Katrin Plenkers[3], Juliane Starke[1], Felix

Blümle[1,4], Christoph Janssen[1],Georg Dresen[1]

[1]Helmholtz Centre Potsdam, GFZ German Research Centre for Geosciences, Section 4.2: Geomechanics and
Scientific Drilling, Telegrafenberg, 14473 Potsdam, Germany
[2]GmuG mbh, Bad Nauheim, 61231, Germany
[3]ETH Zurich, Bedretto Lab, NO F27, 8092 Zürich
[4]ASIR Seismic GmbH, Aachen, 52062, Germany

Correspondence to: C. M. Boese (carolin.boese@gfz-potsdam.de)

Abstract. In 2018 and 2019, the STIMTEC hydraulic stimulation experiment was conducted at 130 m depth in the
Reiche Zeche underground research laboratory in Freiberg/Germany. The experiment was designed to investigate the
rock damage resulting from hydraulic stimulation and to link seismic activity and enhancement of hydraulic
properties in strongly foliated metamorphic gneiss. We present results from active and passive seismic monitoring
prior to and during hydraulic stimulations. We characterise the structural anisotropy and heterogeneity of the
reservoir rocks at the STIMTEC site and the induced, high-frequency (>1 kHz) acoustic emission (AE) activity,
associated with brittle deformation at the cm to dm-scale. We derived the best velocity model per recording station
from over 200 active ultrasonic transmission measurements for high accuracy AE event location. The average P-
wave anisotropy is 12%, in agreement with values derived from laboratory tests on core material. We use a 16-
station, seismic monitoring network comprising AE sensors, accelerometers, one broadband sensor and one AE-
hydrophone. All instrumentation was removable, providing us with the flexibility to use existing boreholes for
multiple purposes. This approach also allowed for optimising the (near) real-time passive monitoring system during
the experiment. To locate AE events, we tested the effect of different velocity models and inferred their location
accuracy. Based on the known active ultrasonic transmission measurement points, we obtained an average relocation
error of 0.26±0.06 m using a transverse isotropic velocity model per station. The uncertainty resulting from using a
simplified velocity model increased to 0.5–2.6 m, depending on whether anisotropy was considered or not. Structural
heterogeneity overprints anisotropy of the host rock and has a significant influence on velocity and attenuation, with
up to 4% and up to 50% decrease on velocity and wave amplitude, respectively. Significant variations in seismic
responses to stimulation were observed ranging from abundant AE events (several thousand per stimulated interval)
to no activity with breakdown pressure values ranging between 6.4 and 15.6 MPa. Low-frequency seismic signals
with varying amplitudes were observed for all stimulated intervals that correspond to the injection pressure curve
rather than the flow rate. We discuss the observations from STIMTEC in context of similar experiments performed
in underground research facilities to highlight the effect of small-scale rock, stress and structural heterogeneity
and/or anisotropy observed at the decameter scale. The reservoir complexity at this scale supports our conclusion that
field-scale experiments benefit from high-sensitivity, wide-bandwidth instrumentation, and flexible monitoring
approaches to adapt to unexpected challenges during all stages of the experiment.

1 Introduction

Meso-scale, in-situ hydraulic stimulation experiments performed in well-instrumented underground research laboratories (URL) offer a number of advantages over small-scale laboratory tests and reservoir-scale experiments. In particular, URL experiments capture structural heterogeneity on a realistic length scale and are thus essential to transfer results from laboratory tests on centimetre-scale rock samples to reservoir rocks at the kilometre-scale (Young et al. 2000; Gischig et al., 2019). Furthermore, URL experiments allow for validation of inferred results, e.g., through mine-back drilling into stimulated rock volumes (e.g., Warren and Smith, 1985). Most importantly, intermediate-scale, in-situ experiments, conducted in URLs, allow for a close to optimal placement of seismic sensor networks for monitoring and characterisation of the target volume (Ohtsu, 1991; Zang et al. 2017; Amann et al., 2018; Kwiatek et al., 2018; De Barros et al., 2019; Feng et al. 2019). Hydraulic stimulation was seismically monitored during in-situ experiments in various settings (e.g. Ohtsu, 1991; Dahm et al. 1999). The monitoring systems need to be tuned to the seismic waves associated with hydraulic stimulation in terms of sensitivity, frequency range and attenuation characteristics of the reservoir, which limit the detection ranges of the seismic signals (e.g. Mendecki et al., 1999; Plenkers et al. 2010, 2011; Manthei and Plenkers, 2018). Varying noise conditions on site often impact monitoring conditions (Plenkers et al., 2010, 2013). Recently, monitoring of a hydraulic stimulation experiment at 410 m depth at the Äspö Hard Rock Laboratory (AHRL) in southern Sweden in May/June 2015 (Zang et al., 2017; Kwiatek et al., 2018) showed that only two of the multiple seismic monitoring systems in place were suitable to record the observed seismic processes. The high-sensitivity acoustic emission (AE) network recorded high-frequency (>1 kHz) AE events from fracturing and frictional sliding with rupture dimensions on the centimetre to decimetre scale. A five-station broadband network recorded low-frequency signals of 0.004–0.008 Hz during the frac and refracs. Slow deformation processes have also been monitored with tilt sensors during the "In-situ Stimulation and Circulation Experiment" performed at Grimsel Test Site (GTS) in Switzerland. This experiment was conducted at a depth of 480 m below surface, within an experimental volume of ca. 20 m × 20 m × 20 m of granitic rock between February and May 2017 (Gischig et al., 2018). Dense 3-D coverage and the close proximity of seismic instrumentation to induced AE events both at the AHRL and the GTS sites resulted in high-quality data sets resolving details of the hydro-mechanical processes on the decimetre to metre scale (e.g., Dutler et al., 2019; Kwiatek et al., 2018; Villiger et al., 2020). This level of detail is necessary to advance our understanding of processes relevant for hydraulic stimulations such as (1) hydro-mechanically coupled fluid flow and pore pressure propagation, (2) transient pressure-dependent and permanent slip-dependent permeability changes, (3) fracture formation and interaction with pre-existing structures, (4) rock mass deformation around the stimulated volume due to fault slip, failure processes and poroelastic effects, and (5) the transition from aseismic to seismic slip (e.g. Amann et al., 2018). Currently, AE event distributions provide the most detailed information on small-scale spatio-temporal-evolution of the deformation within the reservoir induced by hydraulic stimulation. In particular, fracture dimensions, orientations, faulting style, and the orientation of the prevailing principal stress axes may be inferred from the analysis of induced seismic events (Manthei et al 2001; van der Baan et al., 2013; Manthei and Plenkers, 2018; Krietsch et al., 2019).

The STIMTEC experiment was designed to develop diagnostic criteria for successful hydraulic stimulations, and to optimise monitoring and stimulation procedures. This experiment was conducted in strongly foliated and

Solid Earth
Discussions

76 heterogeneous metamorphic rock at shallow depth (~130 m). Complementary to the STIMTEC experiment, several

77 other meso-scale injection experiments in crystalline rock are currently underway. The "EGS Collab Experiment" is

78 a multi-institutional collaborative research project at a similar scale that aims to solve technological problems related

79 to EGS-reservoir creation and operation through different stimulation procedures under realistic in situ stress

80 conditions, and to provide a test bed for the validation of existing thermal-hydrological-mechanical-chemical

81 numerical modelling tools (Kneafsey et al., 2018). The second experimental phase is currently planned at the Sanford

82 Underground Research Facility (SURF) at 1.25 km below surface, located in the Homestake mine, a former gold

83 mine in South Dakota, USA (Kneafsey and the EGS Collab Team, 2020; Schoenball et al., 2020). The Bedretto

84 experiment aims at upscaling previous meso-scale experiments by a factor of ten (Gischig et al., 2019) and is located

85 in the Bedretto Underground Laboratory for Geoenergy research (BULG) in Southern Switzerland, about 10 km

86 southeast of the GTS. Current activities aim at stimulating the Rotondo granite at the Bedretto tunnel with an

87 overburden about 1 km thick in an estimated volume of ca. 300 m × 100 m × 50 m allowing to test different

88 hydraulic stimulation as well as seismic and deformation monitoring techniques.

89

90 Site complexity due to small-scale rock stress and structural heterogeneity and/or anisotropy of varying strength and

91 orientation is a major issue encountered by all meso-scale in situ experiments so far. To trace the spatio-temporal

92 evolution of AE events during hydraulic stimulations at high resolution, the accuracy of the applied seismic velocity

93 model for location in anisotropic and heterogeneous rock volumes is of fundamental importance. At the laboratory

94 scale, anisotropic velocity models are commonly applied (e.g., Stanchits et al., 2003). The models are fundamentally

95 important to monitor rock-deformation during laboratory tests at high resolution. At the mine scale, comprehensive

96 and dense in-situ measurements, in particular active seismic surveys, are performed to characterise heterogeneity and

97 anisotropy of the investigated rock volume. These seismic surveys are commonly performed before the stimulation

98 to derive the velocity structure and repeatedly in material science and in-situ experiments to monitor alteration of the

99 rock volume e.g. by fracture generation. Repeated active measurements throughout hydraulic stimulation experiment

100 are still scarce. Their value for monitoring temporal changes resulting from fluid pressure changes in the rock

101 volume has only recently been recognized (Doetsch et al., 2018; Rivet et al., 2016; Schopper et al., 2020). At the

102 field scale, detailed site characterisation is often not possible because of associated costs and limited placement of

103 instrumentation, resulting in velocity model ambiguity and lower resolution of the seismic event distribution. Thus,

104 in STIMTEC we performed resolution tests at the meso-scale to place better constraints on model uncertainties and

105 to provide estimates of the effect of simplifications and approximations required at the field scale.

106

107 The seismic response to stimulation during recent URL experiments was highly variable. At the AHRL site seismic

108 response to stimulation likely depended on rock-type with granodiorite and granite stimulations showing seismicity

109 in contrast to diorite-gabbro host rocks. However, this interpretation is complicated by the fact that three different

110 fluid-injection schemes were applied to test their influence on injectivity and induced seismicity (Zang et al., 2013).

111 At the GTS site, two shear zones (S1, S3) with different deformation history in the Grimsel granodiorite were

112 stimulated. Hydrofrac experiments revealed remarkably different seismic responses north and south of the S3 shear

113 zone in terms of injection pressure, amount of backflow, injectivity before jacking and final transmissivity (see Fig. 4

114 and 5 of Dutler et al., 2019). Villiger et al. (2020) observed differences in the seismicity patterns observed during

115   hydroshear stimulation of the two shear zones. During stimulation of the S1 shear zones, the majority of AE events
116   occurred at the beginning of injection, when the total volume of injected fluid was low, whereas for the S3 shear
117   zone the number of AE events increased with the volume of injected fluid (Villiger et al., 2020). Hydroshear
118   stimulations of the ductile S1 shear zone showed less seismicity overall and larger transmissivity increases than S3
119   hydroshear stimulations. The seismic responses to stimulation during the EGS Collab experiment were also complex
120   (Schoenball et al., 2020). Abundant seismicity accompanied the three hydraulic stimulations at 1.5 km depth at
121   SURF aiming to establish a connection between injection and production boreholes approximately 10 m apart
122   (Kneafsey et al., 2019). Seismicity delineated at least ten planar features with variable orientations that connected to
123   an open natural fracture, which formed a significant fluid pathway and controlled the stimulations (Schoenball et al.,
124   2020).

126   Here, we introduce the STIMTEC project, its monitoring concept and lessons learned from using a 16-station seismic
127   monitoring network for active and passive seismic monitoring during a decimetre-scale hydraulic stimulation
128   experiment in anisotropic and heterogeneous rock. We compare our monitoring experience with other previous and
129   ongoing research experiments in URLs. We review our seismic monitoring strategy, monitoring system adjustments
130   and discuss potential applications to the field scale. We address how anisotropy and heterogeneity are characterised
131   and provide estimates to place better constraints on the effect resulting from simplifications and approximations
132   commonly applied at the field scale.

2   The STIMTEC project
2.1   Objectives, experimental framework, and monitoring strategy

136   The STIMTEC experiment focusses on the development and optimisation of hydraulic stimulation (STIMulation
137   TEChnologies) and aims at establishing the link between damage patterns, hydraulic properties, and observed
138   seismic activity to provide diagnostic criteria for the success of a stimulation (Renner and STIMTEC team, 2021).
139   Therefore, seismic and hydraulic monitoring are key components of the experiment. In addition, validation through
140   mine-back drilling into stimulated volumes of complex rock, small-scale laboratory tests to characterise mechanical
141   and physical properties and numerical modelling are part of the integrated project approach.

143   The STIMTEC experiment comprised the following phases:

- a *pre-stimulation characterisation phase* (including site characterization, borehole drilling and logging, core analysis and hydraulic measurements for interval selection, as well as instrumentation);
- *the stimulation phase* (stimulation of ten selected intervals in the injection borehole during 16–18 July 2018);
- *the hydraulic testing phase* (testing of six intervals in the injection borehole during 8–10 August 2018);
- *the validation phase* (mine-back drilling of three validation boreholes, stress measurements in five intervals of the vertical validation borehole on 21/22 August 2019); and
- *the final hydraulic testing phase* (testing of seven intervals in the injection borehole during 5–8 November 2019).

153   High-resolution seismic monitoring accompanied all experimental phases, but with different foci. During the pre-
154   stimulation characterisation phase, active seismic monitoring aimed at identifying high-attenuation and deformation
155   zones to avoid sensor installation in these zones, to quantify detection ranges, and to obtain a velocity model. The
156   installed sensors were then used to characterise background noise levels and any natural seismicity at the site. During
157   the stimulation phase and subsequent validation phase, real-time passive monitoring aimed at optimised AE event
158   detection, localisation and magnitude estimation during stimulation of intervals in the injection and vertical
159   validation boreholes. Repetitive active seismic measurements were performed along the injection and validation
160   boreholes to investigate any elastic velocity changes resulting from the stimulation. During the final hydraulic testing
161   phase, passive seismic monitoring focused on verifying detection rates observed for some stimulated intervals with
162   few AE event by placing two sensors closer to these intervals.

163

164   **2.2   Site description and infrastructure**
165   The STIMTEC site is located on the second floor of the Reiche Zeche Mine, in the Eastern Ore Mountains beneath
166   the city of Freiberg, Germany at a depth of ca. 130 m below surface (Figure 1). The metamorphic gneiss complex,
167   penetrated by the mine, is referred to as the Freiberger gneiss anticline, and belongs to the Precambrian metamorphic
168   basement of the internal Mid-European Variscan orogeny (Seifert and Sandmann, 2006). It hosts silver, lead and zinc
169   ores, which were mined for centuries (Bayer, 1999). Temperatures at the STIMTEC site are low (~10℃). The
170   protolith of the Inner Grey Gneiss at Freiberg likely was an S-type granite (Tichomirowa et al., 2001, and references
171   therein), which was metamorphosed at about 0.8 to 1.1 GPa and 600 to 700°C and has a Proterozoic age with
172   minimum estimates of 548 to 534 Myrs (c.f. Fig. 11 of Tichomirowa et al., 2001). The fine-grained biotite gneiss has
173   a granitic appearance and often contains large potassium-feldspar porphyroblasts. The mineral composition of
174   Freiberg gneiss is generally characterized by biotite, potassium feldspar, plagioclase, and quartz (Tichomirowa et al.,
175   2001). Freiberg gneiss is a partly weathered, faulted and strongly foliated rock. Large, steeply-dipping mineralized
176   fault zones strike through the gneiss (Sebastian, 2013).

177

178   The monitored rock volume at the STIMTEC site has dimensions of 40 m × 50 m × 30 m and is situated between
179   two galleries: the straight driftway and the curved vein drift that tracks the mined ore lode "Wilhelm Stehender"
180   (Figure 1), a major mineralized fault zone with a thickness of up to 2 m that strikes north and dips westward beneath
181   the site. Large ore lodes at Reiche Zeche are generally considered normal faults and trend predominantly north-south
182   to northeast-southwest. The galleries have a square cross section (width/height of ca. 2 m) and were excavated in
183   1903 (vein drift) and 1950 (driftway).

184

185   In total, seventeen boreholes with uniform radius (76 mm) were drilled in two phases. Eleven seismic monitoring
186   boreholes were completed with a range of orientations and lengths, extending horizontally or upwards from the
187   galleries (Figure 1). The 63 m-long injection borehole was drilled at the maximum inclination angle to the sub-
188   horizontal foliation compatible with seismic monitoring requirements (upwards directed boreholes, possible
189   recording ranges, and placement outside of damage zones). It strikes N31°E and dips 15°. A more steeply inclined
190   (dipping 36°, striking N66°E) hydraulic monitoring borehole was drilled, extending below the central part of the
191   injection borehole with a minimum distance of 2.5 m between the borehole depth 18.4 m in the hydraulic monitoring

192   borehole and 33.9 m in the injection borehole. One cable borehole, connecting the two galleries, was drilled for cable

193   as well as seismic sensor installation. The validation phase comprised mine-back drilling of two inclined validation

194   boreholes of 19.25 m and 45.8 m length, running sub-parallel to the injection borehole and targeting seismically

195   active and inactive volumes (Figure 1), as well as a vertical borehole for evaluation of the stress field. The short and

196   long inclined validation boreholes dip ~12° and ~15°, terminating 3.5 m above and 4.4 m sideways of borehole depth

197   28.1 m and 56.6 m in the injection borehole, respectively. The 15.6m-long vertical validation borehole (dip angle of

198   ~89°) is located in the driftway and spans the same absolute depth range as the injection borehole.

199

200   The STIMTEC site is located 180 m south of the GFZ underground laboratory (Giese and Jaksch, 2016), where

201   extensive site investigations and exploration monitoring in the 10–3000 Hz frequency range have been performed

202   over the last 20 years to characterize the rock mass. The excavation damage zone (EDZ) of the galleries at the GFZ

203   lab may extend up to 10 m into the rock volume with an estimated 7% reduction in P-wave velocity (Krauß et al.,

204   2014). A continuous east-west trending damage zone was seismically imaged showing a ca. 13% P-wave velocity

205   reduction compared to the surrounding rock mass (Krauß et al., 2014). Predominantly east-west trending structures

206   are likely relicts given their orientation with respect to the current regional stress field. The stress field was measured

207   at 140 m depth in the mine, a few hundred metres from the STIMTEC site using an overcoring technique (Table 1;

208   Mjakischew, 1987), suggesting a strike-slip regime with maximum horizontal compressive stress oriented NNW-

209   SSE, which is typical for SE Germany.

210

2.3   Structural analyses

212   Geological structures within the STIMTEC rock volume were identified through mapping of the access galleries,

213   acoustic televiewer images of the injection, hydraulic monitoring and validation boreholes, and from inspection of

214   the recovered core material. This aimed at the detection of possibly continuous fracture systems or damage zones,

215   which could affect the recording of high-frequency acoustic emission events. The foliation was mapped at 34

216   positions and determined to be sub-horizontal to shallowly dipping in a south-east-direction. At least two, east-west

217   trending, steeply-dipping deformation zones were identified in both galleries that occasionally serve as water

218   conduits as indicated by oxidation and Fe_2O_3 deposition in the otherwise intact rock mass. These are referred to as

219   the northern and southern deformation zone. A third zone, the 'middle deformation zone', was predominantly seen in

220   vein drift. Drilling and coring of the injection and validation wells allowed us to check whether these deformation

221   zones actually crossed the entire STIMTEC volume (question mark in Figure 1). The density of open fractures

222   identified from acoustic logs is highest (with 20 fractures per meter) at the bottom of the injection and long inclined

223   validation boreholes, compared to typical values of five open fractures per metre elsewhere. Several prominent

224   structures (at 60 and 62 m) with a range of orientations were identified in the logs from the injection borehole

225   (Figure 2), where the core becomes severely fractured and was not fully recovered. This zone is considered the

226   continuation of the northern deformation zone at depth within the rock volume. Its location and depth is consistent

227   with the orientation of mapped structures in both galleries (Figure 1).

228

229   A connection of the middle damage zone between the driftway and the vein drift is not well constrained. A

230   prominent single fracture is mapped at 32.5 m depth in the injection borehole, also seen at 17 m in the hydraulic

231 monitoring borehole and at 19.8 m in the long, inclined validation borehole (Figure 2). However, this notable

232 structure was not observed in the short, inclined validation borehole. Its interpreted orientation does not match the

233 interpolated position of the middle damage zone based on mapping in the galleries. Ultrasonic transmission

234 measurements from the cable borehole, connecting the two tunnels, indicate that the mapped deformation zone seen

235 in vein drift extends several meters into the rock volume but does not connect to the driftway.

236

237 Between 33–41 m depth in the injection borehole, the number of healed fractures identified from the core is largest.

238 Two prominent structures are seen at 46 and 47 m depth, located in a section of the injection borehole (42–50 m) that

239 contains more fractures on average (Figure 2). The same two structures are likely seen at 38–39 m depth in the long

240 validation borehole.

241

242 Based on the distribution of fractures obtained from core analyses and acoustic image logs as well as hydraulic pre-

243 characterisation results, ten stimulation intervals of 0.75 m length each were selected for stimulation in the injection

244 borehole. Intact intervals were located at borehole depths of 22.4, 24.6, 28.1, 33.9 and 37.6 m (depths reference to

245 the position of the middle of the double-packer probe), while intervals with pre-existing fractures were located at

246 40.6, 49.7, 51.6, 55.7 and 56.5 m depth (Table 2). Four intact sections and one test interval with a pre-existing

247 fracture were selected for stimulation in the vertical validation borehole, corresponding to 4.0, 6.7, 9.3, 11.7 and 13.2

248 m depth (Figure 1).

249

250 **2.4   Hydraulic injection scheme**

251 All selected intervals in the injection and vertical validation borehole were stimulated with a uniform fluid injection

252 scheme:

253 First, a pulse test was performed in the packed-off interval. The test interval was pressurized to assess the

254 performance of the packers and to assess the presence or absence of pre-existing open, conductive fractures.

255 Hydraulic properties were obtained from the time that it takes the pressure to decay from the initial pressure to a

256 certain level (Bredehoeft and Papadopulos, 1980; Cooper et al., 1967). Secondly, fluid was injected into the packed-

257 off interval, maintaining a constant flow-rate and thereby raising the interval pressure until breakdown to create a

258 hydro frac. Once the breakdown pressure was reached the injection was shut-in. Thirdly, three refracs were

259 performed at the same flow-rate as applied during the frac to determine fracture re-opening pressures, to propagate

260 the fracture, and to monitor the evolution of shut-in pressures after each refrac. Subsequently, a step-rate test was

261 performed, comprising stepwise increases of the injected fluid to determine the jacking pressure, when the created

262 fractures changed their state from mechanically closed to mechanically opened. Optionally, a periodic pumping test

263 sequence was performed to derive hydraulic properties, consisting of phases of alternating flow-rates between two

264 levels, ranging from 0.6/1.5 l/min to 6.5/8.5 l/min, for periods varying between 20 s and 900 s (~15 minutes; Table

265 2).

266

267 **2.5   Seismic monitoring network and data acquisition**

268 The seismic monitoring network consisted of 16 sensors, installed in boreholes of 1.5 m to 20 m length to reach

269 beyond the tunnel excavation damage zone. This sensor network was used for both active seismic measurements and

270   passive seismic monitoring. We used 12 *GMuG[1] MA BLw-7-70-75* AE side-view single-component in-situ AE
271   sensors that provided high sensitivity in the frequency range 1–100 kHz, allowing to detect AE events with rupture
272   plane dimensions in the cm- to dm-scale (cf. Kwiatek et al., 2011; 2018). The AE sensors were placed in upwards
273   pointing boreholes located above the injection well, reducing the risk of sensor failure due to water intrusion.
274   Minimum sensor distances to the stimulation intervals in the injection borehole were 5.3–19.7 m (Figure 1, c.f. Table
275   2 for average distances). The spatial coverage of the sensors was optimised for event detection, determination of
276   hypocentres and focal mechanisms (cf. Plenkers et al., 2010; Kwiatek and Ben-Zion, 2016), based on results
277   obtained from an active seismic survey performed in the pre-stimulation characterisation phase. This survey showed
278   a strong influence of deformation zones on the amplitude and frequency content recorded by the AE sensors and
279   placed constraints on maximum recording distances. Given the limitations regarding the number of monitoring
280   stations and expected strong damping of elastic waves, we realised that not all parts of the injection borehole could
281   be equally well monitored. We therefore focussed the seismic monitoring on the intermediate-depth range (25–35 m
282   depth) of the injection borehole. However, we decided to drill two monitoring boreholes longer than required for the
283   preferred network design to allow for changes in sensor placements, if necessary. In addition, one channel of the
284   datalogger was left available for flexible use and testing onsite.

285

286   Three AE sensors were co-located with uniaxial *Wilcoxon 736T* accelerometers with sensitivity between 0.05–25
287   kHz for the in-situ calibration of the AE sensors (cf. Plenkers et al., 2010; Kwiatek et al., 2011, 2018). In addition, a
288   six-component *ASIR[2] A-SiA-ULN-G4.5-GS-70* broadband sensor was installed in a borehole to extend the range of
289   recorded signals to low frequencies. It consists of a three-component 4.5 Hz geophone and a three-component ultra-
290   low noise optical accelerometer with sensitivity in the range 0.01–100 Hz. This borehole sensor is noisier in the
291   frequency band 0.01–10 Hz but less noisy for 10–100 Hz compared to the Trillium Compact 120 s broadband
292   sensors installed in the AHRL tunnels, which recorded low-frequency signals associated with the frac and refracs
293   (Zang et al., 2017). One component of the sensor was simultaneously recorded on the high frequency AE system data
294   logger (using the one channel available for flexible use during pre-stimulation and stimulation phases) and by a low-
295   frequency six-channel broadband system data logger (during all experimental phases) for synchronous timing and
296   data matching. The broadband sensor was first installed in a 1.5 m long sub-horizontal borehole in the vein drift, but
297   was then removed and modified for installation in the 15 m- deep vertical validation borehole in the driftway. By
298   placing the sensor closer and at a comparable absolute depth to the deepest stimulation intervals in the injection
299   borehole, we wanted to test if it recorded signals associated with stimulation and hydraulic testing of these intervals.

300

301   A *GMuG HAE40k* sensor, hereinafter referred to as an AE-hydrophone, because of its characteristics somewhat
302   similar to an hydrophone and suitable for in-water installation, was installed in the down-going hydraulic monitoring
303   borehole for the final hydraulic testing phase, and connected to the available channel for flexible use. This
304   piezoelectric AE-sensor is sensitive to pressure changes in the frequency range 1–40 kHz and was added to the

---

[1]Gesellschaft für Materialprüfung und Geophysik (www.gmugmbh.de)
[2]Advanced Seismic Instumentation and Research LLC (www.asirseismic.com)

305 network to provide a high-sensitivity sensor in close proximity (6–17 m) to the intermediate and deep stimulation

306 intervals.

307

308 Seismic waveforms were recorded with the *GMuG AE System* datalogger, a 16-channel, 16-bit acquisition system

309 that allowed recording both in trigger-mode with a sampling frequency of 1 MHz as well as in continuous mode with

310 sampling frequency of either 200 or 500 kHz. The six channel data logger of the broadband system recorded

311 continuously at 125 Hz during the initial stimulation and hydraulic testing and 1000 Hz during the final hydraulic

312 tests. By using a continuous and a triggered seismic monitoring system simultaneously, data redundancy and

313 different data accuracy was obtained. The two seismic monitoring modes can be easily switched from one to the

314 other, allowing for flexible use for active (up to 32 channels, in triggered mode) and passive seismic monitoring (16

315 channels, both modes).

316

317 **2.6   Active seismic measurements**

318 For active measurements three different sources, capable of generating high-frequency signals in the kHz range, were

319 used. A survey, comprising sledge-hammer hits at 84 fixed positions in the vein drift recorded by four AE sensors

320 located in the driftway, was performed during the pre-stimulation characterisation phase. Each hit was also recorded

321 by a sensor fixed to the hammer, providing the origin time. These recordings were used to test the transmission of

322 elastic waves across the test volume and to obtain an estimate of the influence of deformation zones on the amplitude

323 and frequency content recorded by the AE sensors at varying recording distances. Together with the structural

324 analysis at the site, these measurements were used to determine final sensor placements of the seismic monitoring

325 system, omitting high-attenuation and deformation zones.

326

327 Similar active measurements were repeatedly performed at 24 fixed points in the vein drift and the driftway before,

328 during and after all other phases of the experiment (Figure 3) using sledge hammer and centre punch tools. To obtain

329 origin times for some of these hits, an additional accelerometer was installed next to the hitpoint. Centre punch tools

330 generate a more repeatable signal than the sledge hammer, with a defined impact force controlled by the internal

331 springs. We used three different centre punches with spring forces adjusted to 50N, 130N, and 250N. The spectra of

332 the generated impulse signals partially overlap with the spectra of AE events, containing higher frequencies

333 compared to the hammer impulse (Supplement material Figure S1). These hits, recorded by all AE sensors and

334 accelerometers, form an extensive dataset for AE sensor calibration, site attenuation and are a pre-requisite for

335 estimating magnitudes of the AE events (Kwiatek et al., 2011).

336

337 Sledge hammer hits also served as a simple reference signal to mark critical monitoring periods during all phases of

338 the experiment: Three hammer hits before the start and three to six hits at the end of each hydraulic pumping

339 operation allowed to calibrate timing of the seismic and hydraulic observation systems, made different groups on site

340 (located in different galleries during the stimulation) aware of operations and helped to distinguish working noise

341 from the target AE signals.

342

343   In addition to the active surveys along the tunnel walls, >300 ultrasonic transmission (UT) measurements were

344   performed in the hydraulic monitoring, injection, validation, and cable boreholes for velocity model estimation. The

345   ultrasonic transmitter (central frequency ~15 kHz) discharged a delta pulse of 7 μs duration. A total of 1024 of these

346   pulses were automatically stacked on each sensor channel to improve the signal-to-noise ratio. The resulting signal

347   generally contains more high frequency energy than common AE signals (>30 kHz, Supplement material Figure S1).

348   UT measurements in the injection borehole, with sources placed every metre along most of its length, were

349   performed for velocity measurements before and after the stimulation. The ultrasonic transmitter was placed in three

350   different orientations before the stimulation and at one orientation after the stimulation. The vertical validation

351   borehole was also sounded before and after stimulation, while the remaining validation and cable boreholes were

352   sounded once at the end of the validation phase or the final hydraulic testing phase of the experiment, respectively

353   (Figure 3).

354

355   **2.7   Passive seismic monitoring**

356   To monitor injection-induced fracture processes and associated small-scale brittle rock failure, we focussed passive

357   seismic monitoring on small magnitude ($M_W \leq -1.5$), high frequency ($f \geq 300$ Hz) AE events with expected fracture

358   sizes ranging from a few cm to the m-scale (Bohnhoff et al., 2010). Similar monitoring was previously successfully

359   applied (see review by Manthei and Plenkers, 2018; Kwiatek et al., 2018; Villiger et al., 2020).

360

361   Passive seismic (continuous and triggered) data were recorded during all injection operations. Triggering levels were

362   adjusted during hydraulic pumping operations and tuned for each stimulation interval to minimize false triggers that

363   lead to a dead time in the triggered recording system. Noisy channels were switched off to facilitate monitoring of

364   many partly overlapping AE events in real-time on site and to identify larger events. AE events detected in trigger

365   mode were automatically picked and located in near-real time on-site to obtain a pre-liminary catalog and control the

366   experiment. Outside of stimulation campaigns, the continuous-mode system was operated between 29 June and 14

367   August 2018 (with some data gaps, see Supplementary Material Table S1) and 5 November to 4 December 2019 (no

368   gaps) to measure post-stimulation processes and to characterize potential background seismicity. We recorded >72

369   TB of seismic data by the end of the field experiment.

370   **3   Methods**

371   **3.1   Data processing**

372   The different phases of the STIMTEC experiment were accompanied by varying in-situ noise conditions that

373   affected predominantly the high-sensitivity AE sensors. Passive seismic data often showed contamination with

374   transient electronic noise and noise generated by the hydraulic pumps during stimulation. To address this problem,

375   we applied filtering using the continuous wavelet transformation. We first identified the wavelet coefficients related

376   to transient noise signals by comparing continuous seismic data with and without noises. By removing the identified

377   wavelet coefficients from the recorded wavelet spectrum, the unperturbed AE signal could be retrieved efficiently.

378   This was possible because AE signal and noise overlapped only partially (Supplementary material Figure 2).

379

380   For post-processing of the triggered AE event data, we apply the automatic phase identification algorithm by Wollin

381   et al. (2018), which is based on the two-step approach by Küperkoch et al. (2010) to first determine a preliminary

382   arrival time, which is then refined by suppressing noise and using a wider causal band-pass filter. The waveforms are

383   first filtered using a third order Butterworth bandpass filter before a rolling higher-order-statistics kurtosis filter is

384   applied to determine a preliminary onset time. Then, by systematically calculating suits of Akaike's information

385   criterion (AIC)-functions on rolling and nested time windows of wavelet portions containing the phase onset, the

386   variability of the global minima is used to estimate the final pick as well as an asymmetric pick uncertainty.

387   Parameter settings are given in Table 3. The same procedure is applied for P- and S-arrivals. However, given the

388   single-component data and the AE sensor's typical post-pulse oscillations, automatically picked S-arrivals are

389   considered uncertain in this study. We observed that the amount of automatically picked S-arrivals is significantly

390   larger than for a reference dataset of manually picked S-arrivals. The reference dataset, comprising 300 events with

391   2,286 manual P- and 1,021 S-picks, was used to tune the automatic picking algorithm.

392

3.2   Velocity model

394   We used the active seismic UT measurements to derive a velocity model. UT data were manually inspected and

395   arrival times of the P- and S-waves, as well as the origin time of the UT source pulse, were identified. We

396   distinguished between impulsive, high-signal to noise ratio P-wave arrivals and more emergent, low-signal to noise

397   ratio onsets, with the latter being down-weighted by 50% for relocation and other procedures. Given the known

398   origin time and location of each UT measurement point, travel times to the seismic sensors were calculated assuming

399   straight ray paths. Uncertainties of the obtained velocities were assessed from repeated measurements from each

400   point in the injection borehole.

401

402   The Freiberg gneiss displays a prominent sub-horizontal foliation and was expected to show transverse isotropic

403   elastic properties as seen from core measurements (Adero, 2020) typically showing high P-wave velocities parallel to

404   the foliation and low P-wave velocities perpendicular to it. To describe the observed anisotropy of the obtained

405   velocity values, we applied the exact phase velocity equations for transverse isotropy (Thomsen, 1986, equations 10

406   a-d):

407
$$v_P^2 = v_{P0}^2 \ [1+ \varepsilon\sin^2\theta + D^*(\theta)],$$

408
$$v_{SV}^2 = v_{S0}^2 \ [1 + (v_{P0}/v_{S0})^2 \varepsilon\sin^2\theta - (v_{P0}/v_{S0})^2 D^*(\theta)],$$

409
$$v_{SH}^2 = v_{S0}^2 \ [1+2\gamma\sin^2\theta],$$

410   where ε and γ describe the strength of anisotropy for P-waves and for S-waves, respectively, v_{P0} or v_{S0} are velocities

411   along the symmetry axis, and θ is the phase angle. The parameter D^* is defined as

412    $D^*(\theta) = 0.5[1-(v_{S0}/v_{P0})^2]\{[1+4\ \delta^*\sin^2\theta\cos^2\theta/(1-(v_{S0}/v_{P0})^2)^2 + 4(1-(v_{S0}/v_{P0})^2 + \varepsilon)\ \varepsilon\sin^4\theta\ /(1-(v_{S0}/v_{P0})^2)^2]^{0.5}-1\}$,

413   with:

414    $\delta^* = (1-(v_{S0}/v_{P0})^2)\ (2\delta-\varepsilon)$

415   The angular dependence of the velocity is given by the shape factor δ.

416   Using the full description is significantly more complex than the weak anisotropy approximation:

417
$$v_P^2 = v_{P0}^2 \ [1+ \delta\sin^2\theta \cos^2\theta + \varepsilon\sin^4\theta],$$

418
$$v_{SV}^2 = v_{S0}^2 \ [1 + (v_{P0}/v_{S0})^2 \ (\varepsilon - \delta) \sin^2\theta \cos^2\theta],$$

419
$$v_{SH}^2 = v_{S0}^2 \ [1+2\gamma\sin^2\theta],$$

420   which was derived by Thomsen (1986) for weak-to moderate strength of anisotropy (ε, γ<0.2). This approximation is

421   commonly applied and describes the actual transverse isotropy accurately along and perpendicular to the symmetry

422   axis but not at intermediate angles.

423

424   We determined Thomson's anisotropy parameters for P-waves (v_{P0}, ε, δ) for each seismic station assuming full

425   transverse isotropy with a vertical symmetry axis. There was no angular asymmetry observed in the measured

426   velocities that would indicate a tilt of the symmetry axis. We assume that the recorded wave velocities represent

427   phase velocities rather than group velocities. We first calculated all wave velocities by systematically varying ε, δ in

428   steps of 2% and v_{P0} in 100m/s steps. Then, the residual between computed and measured P-wave velocities were

429   computed in a comprehensive grid search over the sampled parameter ranges. Due to the scarcity of S-wave

430   observations in the UT data, the ratio of P-to-S wave velocities (v_{P0}/v_{S0}) along the vertical symmetry axis and the S-

431   wave velocity anisotropy parameter γ were fixed to 1.77 and 18%, respectively. These estimates were based on

432   Wadati (1933) plots for near-vertical ray paths and sonic logs from a 70 m-long, vertical borehole of the GFZ lab

433   (Giese and Jaksch, 2016). This sonic log shows the average value at shallow and deep depths, but a large deviation

434   for intermediate depths. The v_{P0}/v_{S0} value is slightly larger than the average value obtained from the sonic log in the

435   (15°-inclined from horizontal) injection borehole. Both logs exhibit large scatter (±0.15). To determine the set of best

436   fitting Thomsen parameters per station (Table 4), we compared the parameter ranges for the best 10 and 100 models.

437   This velocity model was referred to as the best transverse isotropic velocity model per station. It was compared to an

438   isotropic velocity model (v_P=5600 m/s, v_P/v_S=1.76) and a single transverse isotropic velocity model for all stations

439   (v_{P0}=5300 m/s, ε=11.3%, δ=0, v_{P0}/v_{S0}=1.76).

440

441   To clarify limits on the detection ranges as a function of distance, attenuation and anisotropy at the decameter scale,

442   we investigate attenuation characteristics of the rock. Attenuation estimates of the elastic waves travelling in the fast

443   anisotropy direction parallel to the foliation were obtained using hammer and centre punch hits. For each of the 10

444   hammer hits at each hitpoint along the galleries, an 8 µs time window starting at the P-arrival was chosen, from

445   which the maximum amplitude value was extracted. Then, the dominant frequency of the signal was determined for

446   each AE sensor from the maximum amplitude in the frequency range containing 99% of the energy of the signal. The

447   average of the dominant frequency from all sensors f_{dom} together with the slope of the regression line m of the log of

448   the amplitudes with distance from the hitpoint and the average S-wave velocity v_{S90} in the horizontal direction was

449   used to estimate the quality factor Q, according to:

450   $Q=|\pi f_{dom}/(m\ v_{S90})|$.

451   Also, attenuation estimates were obtained by comparing waveforms of centre punch hits recorded by accelerometers

452   located in opposite galleries with one sensor next to the hitpoint. Spectral ratios were analysed to obtain an estimate

453   of the quality factor.

454

455   **3.3   Hypocenter locations and velocity model uncertainty**

456   During post-processing hypocenter locations were determined using the equal differential time (EDT) method by

457   Zhou (1994) combined with a downhill simplex optimization algorithm (Nelder and Mead, 1965) applying the

458   developed transverse isotropic velocity model derived for each station. The EDT method has the advantage that the

459   inversion of the hypocenter location is based on the relative arrival-times of pairs of P- and S wave arrivals at the

460   same station or pairs of P-arrivals at different stations. The origin time is not specifically inverted for, but obtained as

461   a by-product. Gischig et al. (2018) demonstrated how the inversion for origin time, hypocenter location and station

462   corrections are affected by anisotropy. Applying the weak anisotropy approximation, these authors calculated the

463   velocity-dependent derivatives required for the inversion. We did not specifically account for anisotropy in the

464   location procedure, because the non-linear EDT method can handle 3-D heterogeneous velocity models. Instead, we

465   used the anisotropic velocities in the forward computation of the calculated travel-time grids, from which the EDT

466   surfaces were determined. We tested the method by relocating the known UT measurement points using the

467   manually identified P-arrival times with the derived velocity model per station.

468

469   To locate the AE events, we derived an initial hypocentre location based on P-wave arrivals only and a final location

470   including only those S-arrivals, consistent with the initially-derived hypocenter. To be included in the location

471   procedure, the root-mean-squared (rms) residual for an S-arrival needed to be less than 1.5 times the rms of the P-

472   arrivals for the initially derived hypocenter ensuring that inaccurate autopicked S-arrivals were discarded. The rms is

473   defined as

474    $rms=(\sum_i (t_i^{calc} - wt_i^{obs})^2 / \sum_i)^{0.5}$,

475   where t_i are calculated and observed travel times for i stations and w is the weight. Phase weighting for autopicked P-

476   arrivals was implemented, based on the signal-to-noise ratio (SNR), with SNR≥6 obtaining full weight, 6>SNR≥3

477   half weight and SNR<3 one tenth of the full weight. S-arrivals were weighted with two tenth of the full weight if

478   included in the hypocenter estimation. We consider only events with a minimum of five phase arrivals and display

479   those hypocenter locations with rms travel time-residuals below a selected limit of 2 ms. We also applied station

480   residuals obtained as average P-wave travel-time residuals per station.

481

482   To assess the influence of the applied velocity model on the hypocenter locations, we compared the median rms

483   travel-time residuals of all AE event hypocentres obtained using different velocity models as well as the location

484   uncertainty of the relocated UT measurement points. By comparing the relocation error from the isotropic velocity

485   model with the transverse isotropy model and the best transverse isotropic velocity model per station, we provide

486   estimates for the location uncertainty associated with inaccurate velocity models.

487   **4   Results**

488   **4.1   Constraints on velocity models and location uncertainty**

489   Using a transverse isotropic velocity model per station, we obtained more accurate locations (lower rms travel-time

490   residuals, Table 5) and reduced the uncertainties determined from re-locating the known UT measurement points

491   (using the manually identified arrival times and the derived v_P- and v_S-velocities, Figure 4) compared to using an

492   isotropic velocity model or a single transverse isotropic velocity model for all stations. The latter was determined

493   from the averaged Thomsen parameters of all stations (Table 5). The best velocity model per station results in an

494   average relocation error of 0.26±0.06 m for the active seismic UT measurement points in the range 22–31 m

495   borehole depth in the injection borehole (Figure 4b), along which the majority of AE events were observed,

496   compared to 2.6±0.20 m for isotropic and 0.49±0.12 m for the single transverse isotropic velocity model. Relocation

497   of the UT measurement points was based on using only P-arrival times. Adding the S-wave arrivals did not further

498   reduce the location errors. This is likely because there are only few S-picks (on average 3 per measurement point for

499   the injection borehole and 5 for the vertical validation borehole, compared to on average 12 and 13 P-picks)

500   identifiable in the UT data. Note that the S-wave velocity model is not well constrained, but the few S-arrivals

501   observed in the active UT dataset are consistent with the assumed S-anisotropy parameters (v_{S0}, γ).

502

503   The best transverse isotropic velocity model per station also provided the lowest relocation error on average along

504   the injection borehole outside the damage zone (borehole depths <42m), where the resolution accuracy is decreased

505   by 70% for the isotropic model and 29% for the single transverse isotropic model (Table 5), respectively. We

506   observe that the best velocity model per station is tuned to the injection borehole because its number of measurement

507   points is largest. For relocating the known UT measurement points in the vertical validation borehole, relocations

508   obtained using the single transverse isotropic model (average relocation error of 0.69±0.53 m, Figure 4b) are more

509   accurate than for the best velocity model per station (average error 0.95±0.46 m). The isotropic velocity model

510   performs best in relocating the known UT measurements in the deformation zone based on the relocation error,

511   compared to the anisotropic velocity models. Within the deformation zone, all models show a systematic mislocation

512   upwards above the injection borehole (Figure 4a).

513

514   **4.2   Structural heterogeneity, velocity and attenuation**

515   We investigated the influence of the various geological structures in the rock volume on the seismic wave

516   propagation and on the velocity model. The background anisotropy caused by the strong foliation of the host rock is

517   overprinted by structural heterogeneity on site. We observed significant velocity reductions of 1-4% per station over

518   several UT measurement points (Figure 7a) associated with a prominent fault, identified at 32.5 m in the injection

519   well (Figure 2). We also see significant misfit between the velocities predicted by the anisotropic velocity model and

520   the observed velocities for deformation zones at borehole depths >42 m in the injection borehole and >32 m in the

521   long validation borehole (Figure 3). At these depths the logged structures and elevated fracture densities likely affect

522   seismic wave propagation by strong attenuation and deviating ray paths. This suggests that the velocity models

523   fitting the anisotropic reservoir rocks are inadequate for fault and surrounding damage zones.

524

525   Close to the prominent fault at 32.5 m depth, we observe an amplitude reduction of the stacked UT signal by about

526   50% compared to the values of neighbouring measurement points. This value was determined as the difference

527   between the actual value and the value expected for these depths from linear regression of neighbouring amplitude

528   measurements. Still ambiguity prevails as other factors such as UT source coupling and resonances at the receivers

529   can also affect the recorded amplitudes. In general, we do not observe a systematic velocity or amplitude reduction

530   from UT measurements in the injection borehole after stimulation as compared to before. Attenuation estimates of

531   the elastic waves travelling in the fast anisotropy direction parallel to the foliation obtained from hammer and centre

532   punch hits, resulting in Q_P-factors of about 50 near the galleries and 150 in the centre of the rock mass.

533

534   We observed good SNR ratios for UT measurements in the records of the three accelerometers for distances ≤15–18

535   m. For both accelerometers located off vein drift, we observed clipping of active centre punch hits generated at 10–

536 15 m distance with incidence angles around 90° to the accelerometer axis. This likely reflects resonances and/or

537 coupling issues. UT measurements are not recorded beyond distance of 31 to 33 m by the AE sensors. The AE-

538 hydrophone recorded UT signals with good SNR for distances smaller than 17 m (c.f. Boese et al, 2021). This

539 reduced recording range compared to the AE sensors is likely related to the impedance contrast of the water-filled

540 borehole and the rock. For this reason, AE-hydrophones need to be placed as close as possible to stimulated

541 intervals, or, alternatively, installed permanently by cementation, which reduced the impedance and increases the

542 sensitivity.

543

544 **4.3   Seismic monitoring and network sensitivity improvements**

545 Hydraulic stimulation started in the deepest part of the 63 m-long injection borehole with an intended progression of

546 stimulation from deep to shallow intervals (Figure 1). No AE activity was observed during stimulation of the two

547 deep intervals at 56.5 m and 51.6 m borehole depth, closest to the highly fractured damage zone encountered at the

548 bottom of the borehole. These intervals locate furthest from the seismic monitoring network (HF1 and HF2; Table 2).

549 To test detection limits and the seismic monitoring equipment under the given noise conditions, we changed the

550 intended order of the stimulated intervals, so that two shallow intervals (at borehole depth smaller than 30 m: HF3

551 and HF4) were stimulated next, followed by two intermediate depth intervals (borehole depth between 30 m and 45

552 m: HF5 and HF6) before returning to the deep intervals (borehole depth greater than 45 m; HF7 and HF8). We

553 observed significant AE activity (several thousand events, Table 2, Figure 5 and Figure 6a) for the shallow

554 stimulation intervals (22.4 m, 24.6 m, and 28.1 m) and high breakdown pressures (11–13 MPa). Seismic activity was

555 not identified before the start of the stimulation and stopped after shut-in. Few AE events were recorded during

556 injection into intermediate-depth intervals (33.9 m, 37.6 m and 40.6 m depth, Table 2). These events occurred

557 diffusely throughout the pumping sequence (Figure 6b). For the interval 33.9 m the second lowest breakdown

558 pressure (6.4 MPa) of all tests was observed, whereas the adjacent interval 37.6 m exhibited the highest observed

559 value (15.8 MPa), pointing towards significant spatial complexity. The breakdown pressure of interval 40.6 m (9.4

560 MPa) is comparable to those in the deep intervals 49.7 m, 51.6 m, 55.7 m, 56.5 m, which show intermediate to low

561 values (5.8–9.4 MPa, Table 2) and no AE events, neither during the stimulation nor during subsequent hydraulic

562 testing phases of the experiment.

563

564 For stimulations of the seismically active intervals in the injection borehole (HF3, HF4, HF10; Table 2) and in the

565 vertical validation borehole (HF12-15; Table 2, Figure 5), we observed a general correlation between seismicity,

566 fluid-injection cycles and volumes, when the injection pressure exceeded the fracture opening pressure. A small

567 number of AE events occurred during the frac and refrac sequences (5–70 AE per sequence), whereas significantly

568 more events were observed during subsequent step-rate tests (75–180 AE above jacking pressure) and during

569 periodic pumping tests (30–240 AE per cycle, Figure 6). We observed a progressive growth of the seismic clusters

570 which extend about 5 m radially from the injection interval (Figure 5). The sub-horizontal foliation does not seem to

571 noticeably influence event propagation and seismic cloud growth. Note that the seismic clusters from the injection

572 and vertical validation borehole are spatially distinct.

573

574   The highly variable seismic response to stimulation prompted us to relocate two of the 16 seismic monitoring sensors
575   (Figure 1) to test if the absence of AE activity results from limitations in network sensitivity or site characteristics.
576   We placed one AE-hydrophone at the bottom of the hydraulic monitoring borehole to verify AE detection levels for
577   intermediate-depth and deep stimulated intervals in the injection borehole. The AE-hydrophone recorded few AE
578   events during further hydraulic testing and accidental re-stimulation of the intervals 37.6 m and 40.6 m (at 6–8 m
579   hydrophone-interval distance), respectively, but no activity was observed for intervals 49.7 m and 56.5 m (at 10 m
580   and 17 m distance), confirming previous observations of no AE activity in the deep stimulation intervals. The
581   borehole broadband sensor was moved to the bottom of the vertical validation borehole for the last phase of the
582   experiment, so that it located at a comparable absolute depth as the deepest stimulated intervals in the injection
583   borehole. This was considered beneficial because of indications that seismic wave attenuation perpendicular to the
584   foliation may be larger than parallel to the foliation (Adero, 2020). Overall, the broadband sensor recorded
585   characteristic signals during hydraulic stimulations of all intervals in the injection borehole on 16-18 July 2018
586   (Figure 7 and Supplementary Material Figure 3) that resemble the injection pressure rather than the flow rate. These
587   signals were not recorded by the only other nearby broadband sensor FBE (SX Net, distance 438 m SE of STIMTEC
588   site). The observed signals vary in amplitude and period and are best observed on bandpass filtered (0.001–1 Hz)
589   daily seismograms on the second horizontal component of the ASIR sensor, likely aligned parallel to vein drift
590   (perpendicular to the borehole). There are also spike signals observed that may indicate rapid tilting and recalibration
591   of the sensor (see also Supplementary material Figure 3), based on shake table calibration after the experiment. They
592   occur during operations at the site and their interpretation currently remains unclear.

593   **5   Discussion**
594   **5.1   Seismic monitoring and network adaptions**
595   Using a seismic monitoring system consisting of AE-hydrophones, AE sensors, accelerometers and broadband
596   sensors bears several advantages. The AE-hydrophone can be attached on hydraulic tubing and therefore installed in
597   combination with hydraulic equipment. This places it much closer to the stimulated intervals and as a consequence,
598   AE-hydrophones can enlarge the 3-D density of sensors and their coverage in the volume of interest, thus improving
599   location accuracy and focal mechanism determination. AE-hydrophones do not require coupling to the rock mass and
600   are more easily installed than AE sensors. This comes at the cost of reduced recording ranges and frequency
601   bandwidth compared to common AE sensors (and reduced S-wave sensitivity cf. Boese et al., 2021).

602

603   All dedicated seismic monitoring boreholes were located above the stimulated volume to ensure that water entering
604   into the boreholes can drain during the experiment. This posed the general problem of increased location uncertainty
605   in the vertical direction. However, with this setup we achieved the desired monitoring quality without needing an
606   extra monitoring borehole placed close to the stimulation borehole. During the EGS Collab and GTS experiments,
607   the intersection of growing fractures with nearby monitoring boreholes caused immediate pressure release, inhibiting
608   fracture growth (Schoenball et al., 2020). This illustrates the problem that monitoring boreholes may impinge on the
609   stimulation. Therefore, high sensitivity AE sensors placed at some distance (20–30 m, considering the site
610   characteristics of the STIMTEC experiment) to the stimulated intervals combined with AE-hydrophones placed close
611   to the stimulated interval in the stimulation borehole (above the double packer) likely offer the best solution for high-

612 resolution seismic monitoring during hydraulic stimulation in URLs. However, preservation of the high-frequency

613 content of seismic waves is site dependent and a prerequisite for the analysis of source properties of AE events with

614 expected fracture sizes at the dm-scale (e.g. Kwiatek et al., 2011). Empirical results of Plenkers et al. (2010) provide

615 upper bounds for detection limits of AE events in low-attenuating hard rocks at ~3 km depth. In the more general

616 case, we refer to the modelling of detection limits for high frequency energy of microseismic events by Kwiatek and

617 Ben-Zion (2016).

618

619 Adapting the stimulation on site by changing the stimulation order in the injection borehole allowed for testing the

620 sensitivity of the monitoring system and site conditions but also resulted in the stimulation of the most seismically

621 active intervals (HF3, HF4, HF10; Table 2, Figure 5) on three subsequent days. This adaption was possible because

622 of the near real-time processing and visualisation of AE events on site. It allowed us to separate the temporal

623 distribution of the AE events in the spatially overlapping seismicity clouds (Figure 5).

624

5.2   Seismic response to stimulation

626 We observed significantly different seismic and hydraulic responses of intervals separated by only a few meters in

627 heterogeneous, metamorphic rock (Figures 5 and 6). This generally agrees with observations from the AHRL, GTS

628 and EGS Collab experiments, which also highlighted the influence of the rock type, the pre-existing fracture zones,

629 and stress heterogeneity on seismic responses to hydraulic stimulation. Although it is not yet clear what causes the

630 large variability in deformation behaviour at the STIMTEC site, we verified that it is not the result of detection

631 capabilities of the seismic monitoring network along the injection borehole. We posit that deformation in response to

632 stimulation in the deepest part of the injection borehole is predominantly aseismic, based on the absence of AE

633 events and the strong long-period signal recorded by the broadband sensor. We suspect the observed variability in

634 seismic response to stimulation is likely caused by rock-mass heterogeneity and the response of pre-existing

635 fractures. In addition, injection boreholes not aligned with one of the principal stress axes show complex fracture

636 initiation (Rummel, 1987; Haimson and Cornet, 2003), likely controlled by small-scale material heterogeneities at

637 the borehole wall, as also observed in lab experiments (Masuda et al., 1993). Reorientation of fractures with growth

638 away from the injection interval has been observed previously in boreholes misoriented with respect to the principal

639 stress axes, for example by mine-back in soft volcanic rock (Warren and Smith, 1985) and by AE event cluster

640 orientations in crystalline rocks (Gischig et al., 2018; Schoenball et al., 2020) and salt rock (Manthei et al. 2001). Re-

641 orientation of AE event clouds has not yet been identified during the STIMTEC experiment. We note, however, that

642 unexpected (based on stress modelling), strong, local variations of the stress magnitudes in the experimental volume

643 were obtained from direct stress measurements in the injection and vertical validation boreholes (Adero, 2020). The

644 variability of shut-in pressures (with the largest deviations from the average values observed in the adjacent

645 stimulation intervals at 33.9 m and 37.6 m depth in the injection borehole) and orientations of induced fractures

646 suggest overall small-scale stress heterogeneity at the STIMTEC site (Adero, 2020).

647

648 The observed low-frequency broadband recordings are similar to those broadband records observed by Zang et al.

649 (2017, their Figure 11) at the AHRL. In particular, we obtained strong signals from stimulations that did not yield

650 high frequency AE events. However, not all observed pressure peaks can be correlated with peak amplitudes of those

651   low-frequency seismic signals, suggesting that there seems to be a complex relationship, dependent on pressure

652   amplitude and period that requires further investigation. Our observations suggest that borehole sensors sensitive in

653   the frequency range 0.01–100 Hz positioned at distances of 19.6–26.6 m are adequate to monitor low-frequency

654   deformation associated with hydraulic stimulations.

655

656   **5.3   The role of anisotropy and heterogeneity for mine- and lab-scale experiments**

657   Laboratory and active seismic measurements from the STIMTEC experiment show moderate to strong elastic wave

658   anisotropy controlled by the pronounced foliation of the gneiss. We compare the here obtained Thomsen parameters

659   to those values determined in a range of laboratory tests on cylindrical Freiberger gneiss samples at different

660   confining pressures (≤30 MPa) and orientations at room temperature (Adero, 2020). P-wave velocity measurements

661   on samples in the laboratory exhibit similar mean values and ranges for wave propagation in different orientations

662   with respect to the foliation as observed in field measurements (Figure 8). This is irrespective of the significant

663   differences in frequency bands of UT sources in the laboratory (500 to 800 kHz) and in the mine (5 to 60 kHz). At

664   the STIMTEC site, P-wave velocities for ray paths parallel to the foliation are on average 12% higher than

665   perpendicular to the foliation for UT data. In laboratory tests, P-wave velocities for ray paths parallel to the foliation

666   are slightly larger, about 20% higher compared to a direction normal to the foliation (Figure 8, Table 1). A large

667   amount of active UT field measurements was needed to cover the range of incidence angles necessary to determine

668   the degree of P-wave velocity anisotropy and the symmetry axis of the metamorphic rock (Figure 3). Near-vertical

669   ray-paths (parallel to and at acute angles to the symmetry axis) were difficult to obtain due to geometrical constraints

670   limiting sensor positioning. In general, we observed a trade-off between the obtained P-wave velocity along the

671   symmetry axis v_{P0} and the P-wave anisotropy parameter ε for the UT data (Supplementary material Figure 4). This

672   likely is an effect of missing constraints near the symmetry axis because of few near-vertical ray paths for the

673   majority of stations. The two stations located furthest above the injection borehole with the highest number of near-

674   vertical incidence angles, display intermediate ε values of 8–12% and v_{P0}=5200-5400 m/s. The average velocities of

675   v_{P0}=5275 m/s and v_{S0}=2980 m/s from a sonic log for comparable depths in the vertical borehole of the nearby GFZ

676   lab is consistent with the obtained velocity models. The average horizontal velocities of v_{P90}=5650 m/s and

677   v_{S90}=3260 m/s from sonic logs in the injection borehole at the STIMTEC site are lower than the average velocities

678   obtained for near-horizontal wave propagation from the UT data (Figure 8). These sonic log velocities are more

679   consistent with P-wave velocities derived for foliation-parallel wave propagation at the GFZ lab. We interpret the

680   lower values to reflect the effect of dispersion, given the frequency content of the measurement (4–30 kHz for sonic

681   log, 0.15–3 kHz for tomography at the GFZ lab, versus 5–60 kHz for active UT at the STIMTEC site).

682

683   Anisotropy complicates the analysis of all measurements in the STIMTEC test volume, especially regarding velocity

684   model calibration and AE event location. In retrospect, we estimate that approximately one third of all active UT

685   measurements in combination with the lab measurements, sonic logging and other available information (Krauß et

686   al., 2010) would have been sufficient to characterise the single transverse isotropic velocity model, which captures

687   the general features of the background anisotropy on site. This implies that the effect of dispersion is insignificant.

688   However, to resolve the best-possible velocity model for each station and to obtain high-accuracy AE event locations

689   required a transverse isotropic velocity model per station, derived from a large amount of active in-situ velocity

690 measurements covering a range of incidence angles. The best velocity model per station leads to a significant
691 location improvement of AE events from the injection and vertical validation borehole as shown by comparing the
692 rms travel-time residuals for different velocity models as well as the relocation error of known active UT
693 measurement points along the boreholes (Table 6). Neglecting anisotropy would lead to significant and systematic
694 location bias by up to 2.6 m (Figure 4b). The average P-wave anisotropy for the STIMTEC site is larger than
695 observed for the granite and granodiorite host rocks at the GTS (~7%) and AHRL but comparable to the phyllites at
696 SURF (Gao et al., 2020). Gischig et al. (2018) showed that at the GTS similar but slightly more scattered AE event
697 clouds could be obtained using the joint hypocenter determination method with an isotropic velocity model and
698 station corrections for AE event locations compared to using the anisotropic velocity model. Their approach is based
699 on the weak anisotropy approximation, but it suggests that the effect of anisotropy can be mitigated this way.
700 However, 32 seismic stations were installed at the GTS and structural heterogeneity is not as pronounced there as at
701 the STIMTEC site, because the shear zones are similar in orientation compared to the foliation causing anisotropy in
702 the rock volume. Our work demonstrates that high-resolution AE event locations (average rms=0.00015 s) can be
703 obtained in heterogeneous rocks with pronounced anisotropy, if an accurate velocity model can be derived. This
704 requires numerous UT calibration measurements from various angles, which is achievable for URL experiments,
705 some computational effort to derive the velocity model and a smart event location procedure. This demonstrates that
706 hydraulic stimulation in complex rock such as anisotropic and heterogeneous metamorphic gneiss is possible and can
707 be monitored (with additional effort), so future in-situ experiments do not need to consider homogeneous rocks only.
708
709 Lab experiments also documented a strong influence of the foliation on the mechanical strength and therefore on
710 fracture propagation and length (c.f. Adero 2020, Vervoort et al., 2014). The shallow depth of the STIMTEC site
711 results in low absolute stress magnitudes (1–6 MPa) and lower differential stress conditions compared to URL sites
712 elsewhere. To limit the effect of the foliation on the stimulation, the injection borehole was drilled at a 16°-angle to
713 the foliation. Despite the low absolute stress magnitudes, neither impression packer marks nor AE cluster
714 orientations indicated that the foliation determined fracture propagation in the injection borehole. This was also
715 found at SURF, where hydro-fractures did not follow the strong foliation but the inclined maximum principal stress
716 over tens of meters in the injection borehole (Oldenburg et al., 2016).
717
718 We observed significant velocity reductions (1–4%) associated with prominent pre-existing structures, in particular
719 in the deformation zones crossing the injection and long inclined validation boreholes (Figure 8). The amplitude
720 reduction of the stacked UT signal at these depth intervals could be 50%. In general, we do not observe a systematic
721 velocity or amplitude reduction from UT measurements in the injection borehole after stimulation as compared to
722 before. We conclude that only prominent pre-existing structures identified in logs have a significant effect (velocity
723 drop larger than the average measurement uncertainty) on velocity and attenuation. Whether transient fluid pressure
724 variations during the stimulation have a measurable effect on velocity (Doetsch et al., 2018) and/ or attenuation at the
725 STIMTEC site remains the subject of further investigations, which will be attempted using relative travel time times
726 from centre punch measurements as opposed to absolute travel times from UT measurements. P-wave attenuation
727 factors determined here for the fast anisotropy direction are generally consistent with the values obtained for the GFZ

19

728   lab (Krauß et al., 2010). Laboratory measurements revealed that attenuation perpendicular to the foliation is stronger

729   than parallel to the foliation (Adero, 2020), but this has not yet been investigated from the obtained field data.

730

731   **5.4   Implications for monitoring field-scale hydraulic stimulation experiments**

732   In field-scale projects, sensor placement is significantly more limited and constrained than in mine-scale settings,

733   where due to the 3D placement of sensors in close vicinity of the injection a close to ideal situation for monitoring of

734   a hydraulic stimulation experiment is achieved (similar to the laboratory scale). By avoiding permanent installations

735   and temporarily removing seismic sensors, we could use the existing boreholes for different purposes throughout the

736   STIMTEC experiment (e.g. for hydraulic monitoring, for passive seismic monitoring using different sensors, for

737   stress measurements, repeating measurements to verify impression packer marks and for repeated active seismic

738   measurements). Accessible boreholes provided us with more flexibility, especially as more boreholes became

739   available during the course of the experiment. Adapting the monitoring (by implementing, testing, and assessing a

740   new AE hydrophone and a broadband borehole sensor) and modifying the order of stimulations proved successful to

741   achieve the monitoring goals of STIMTEC. During a recent geothermal stimulation in Finland adapting the

742   stimulation procedure in response to high-quality real-time monitoring observations was critical for controlling fluid-

743   induced seismicity (Kwiatek et al., 2019). Maintaining flexibility during experiments at the mine and field scale,

744   which have less controlled conditions as compared to lab experiments, is a key element to address surprises and

745   unexpected challenges, which seem inevitable given the higher degree of reservoir complexity observed at these

746   scales. Flexibility requires good on-site communication between the various groups involved in the experiment, time

747   and budget to allow for changes, as well as practical and integrated approaches to manage, exchange, visualise and

748   interpret large 3-D data sets of different formats during the experiment.

749

750   Another observation of fundamental importance was that approximately half of the stimulated intervals were not

751   accompanied by any AE activity, despite appropriate monitoring in-place. Villiger et al. (2020) estimated the amount

752   of aseismic deformation during hydroshear experiments at the GTS and compared this to the amount of seismic

753   deformation, showing that aseismic deformation was dominant for both brittle and brittle-ductile structures. This

754   estimation was based on the total moment, calculated from borehole dislocations of mapped fractures, compared to

755   cumulative seismic moment of AE events and observed cloud extents. Guglielmi et al. (2015), De Barros et al.

756   (2019) and Cornet (2016, and references therein) also showed that deformation is mainly aseismic during

757   stimulations in softer rocks (shales, limestone) at the intermediate scale and sedimentary rocks at the field scale. To

758   simultaneously capture fast and slow deformation processes, which are currently often categorised as either seismic

759   or aseismic due to the limitations of current monitoring systems, requires better high-sensitivity instrumentation with

760   a wider bandwidth. Alternatively, the combination of sensors with different sensitivity and frequency ranges (e. g.

761   AE sensors, broadband, tilt, fibre-optic based strain sensors) is necessary, but requires time synchronisation and

762   amplitude calibration, which can pose sophisticated technical problems (c.f. Zang et al., 2017). To address these,

763   marker signals and regular active seismic measurements proved valuable during the STIMTEC experiment. The

764   mine scale has the advantage that new tools and/or different configurations (numerous sensor arrays) can be more

765   easily tested, and maybe regular high-resolution laser-scan tunnel mapping (Grehl et al., 2015) can be applied as an

766   equivalent tool to InSAR, which was successful in monitoring larger-scale slow- deformation processes at the

767   reservoir scale.

768   **6**   **Summary and conclusions**

769   Meso-scale experiments currently provide the most-detailed in-situ information to further understanding of hydro-

770   mechanical processes associated with hydraulic stimulation and allow for validation of inferred results. In the here

771   presented STIMTEC experiment, conducted in the Reiche Zeche mine URL at 130 m depth, we used a high-

772   resolution seismic monitoring network comprising twelve in-situ AE sensors (for high-sensitivity monitoring of

773   induced seismicity and the recording of active source signals), three accelerometers (for sensor cross-calibration

774   purposes), one broadband sensor (to extend monitoring to the low frequency range) and an AE-hydrophone (to

775   improve the network sensitivity in the deeper rock volume of the experiment). We relocated two monitoring stations

776   and tested new sensors during the course of the experiment to optimise passive and active seismic monitoring. In

777   contrast to other similar experiments, we stimulated strongly foliated rock with pronounced anisotropy during

778   STIMTEC. We acquired a large quantity of active UT measurements for characterising the anisotropy and

779   heterogeneity of the host rock. We monitored in near-real-time small-scale rock failure and friction processes

780   associated with hydraulic stimulation and tracked the spatio-temporal distribution of AE events.

781   Several key observations from the experiment are:

782   We demonstrated that high-frequency (up to 100 kHz) seismic monitoring in complex rock volumes with

783   pronounced anisotropy is possible, if measures are taken to accurately quantify the 3-D anisotropic velocity structure.

784   We applied Thomsen's exact phase velocity equations to deduce a transverse isotropic velocity model per station that

785   accurately locates known active ultrasonic measurement points in the stimulated boreholes. Estimates of

786   simplifications of the velocity structure and neglecting anisotropy significantly affect resolution and range between

787   0.5 and 2.6 m in our experiment.

788   We obtained average Thomsen parameters (P-wave anisotropy of 12%) in agreement with those derived from

789   laboratory and sonic logging data.

790   We observed that rock mass heterogeneity as seen in high-fracture density zones overprint the anisotropy of the host

791   rock and has a significant influence on velocity and attenuation.

792   We observed seismic responses to hydraulic stimulation in ten intervals in the injection borehole, performed with

793   similar injection protocol, ranged from abundant AE activity to no AE activity and are unrelated to monitoring

794   limitations. We attribute the observed variability in deformation to the small-scale rock mass and stress field

795   heterogeneity observed in the injection borehole.

796

797   Our observations indicate that stimulation of strongly foliated and fractured rock mass, such as the Freiberg gneiss,

798   results in activation of a complex fracture network. We infer that most of the induced deformation of the reservoir

799   remains aseismic given the high number of stimulated intervals with little or without AE activity and the observed

800   low-frequency signals recorded by the borehole broadband sensor. Aseismic deformation may be related to injection

801   into open pre-existing fractures in the injection interval; yet, borehole logs do not systematically show pre-existing

802   fractures present in 'quiet' stimulated borehole intervals.

803

Data availability

804

805 All active UT transmission data used in this study, sensor coordinates, measurement recording times and positions as
806 well as manually identified phase arrivals are available from the GFZ data server (https://dataservices.gfz-
807 potsdam.de/panmetaworks/review/fe97aa96c11b9aebca07a838bcb37a99e659ab2280e4045905484df76ae959c1/)
808

809 **Author contributions:**

810 GD conceptualised the experiment and acquired funding for it, GD, GK and KP planned the experiment and its
811 instrumentation, CB, TF, KP, FB and CJ conducted fieldwork, JS and FB helped CB with data curation. CB
812 administered the project, formally analysed the data and lead the investigations. CB wrote the manuscript with
813 feedback and reviewing by GD, GK and KP.
814

815 **Competing interests:**

816 The authors (except TF, KP and FB) state that they are currently employed at the same institution as the
817 journal's chief executive editor Charlotte Krawczyk.
818

819 **Acknowledgements**

825
826

827 **References**

828 Adero, B.: Experimental investigations of mechanical anisotropy of Freiberg gneiss: implications
829 for hydraulic stimulation, Ph.D. thesis, Ruhr-Universität Bochum, 2020.

830 Amann, F., Gischig, V., Evans, K., Doetsch, J., Jalali, R., Valley, B., Krietsch, H., Dutler, N.,
831 Villiger, L., Brixel, B., Klepikova, M., Kittilä, A., Madonna, C., Wiemer, S., Saar, M. O., Loew,
832 S., Driesner, T., Maurer, H., and Giardini, D.: The seismo-hydromechanical behavior during deep
833 geothermal reservoir stimulations: open questions tackled in a decameter-scale in situ stimulation
834 experiment, Solid Earth, 9, 115–137, doi:10.5194/se-9-115-2018, URL https://www.solid-
835 earth.net/9/115/2018/, 2018.

836 Boese, C., Kwiatek, G., Fischer, T., Renner, J., and Dresen, G.: AE-type hydrophone
837 performance during the STIMTEC and STIMTEC-X hydraulic stimulation campaigns at Reiche
838 Zeche Mine, Germany, in: 55th US Rock Mechanics/Geomechanics Symposium, Houston,
839 Texas, USA, 20-23 June, American Rock Mechanics Association, 2021.

840 Bohnhoff, M., Dresen, G., Ellsworth, W., Ito, H., Cloetingh, S., and Negendank, J.: Passive
841 Seismic Monitoring of Natural and Induced Earthquakes: Case Studies, Future Directions and
842 Socio-Economic Relevance, in: International Year of Planet Earth: New Frontiers in Integrated
843 Solid Earth Sciences, p. 414, Springer, Dordrecht, 2010.

844 Bredehoeft, J. D. and Papadopulos, S. S.: A method for determining the hydraulic properties of
845 tight formations, Water Resources Research, 16, 233–238, 1980.

846 Cooper Jr, H. H., Bredehoeft, J. D., and Papadopulos, I. S.: Response of a finite-diameter well
847 to an instantaneous charge of water, Water Resources Research, 3, 263–269, 1967.

848 Cornet, F. H.: Seismic and aseismic motions generated by fluid injections, Geomechanics for
849 Energy and the Environment, 5, 42–54, 2016.

850 Doetsch, J., Gischig, V. S., Villiger, L., Krietsch, H., Nejati, M., Amann, F., Jalali, M.,
851 Madonna, C., Maurer, H., Wiemer, S., et al.: Subsurface fluid pressure and rock deformation
852 monitoring using seismic velocity observations, Geophysical Research Letters, 45, 10–389, 2018.

853 Dahm, T., Manthei, G., and Eisenblätter, J.: Automated moment tensor inversion to estimate
854 source mechanisms of hydraulically induced micro-seismicity in salt rock, Tectonophysics, 306,
855 1–17, 1999.

856 Dutler, N., Valley, B., Gischig, V., Villiger, L., Krietsch, H., Doetsch, J., Brixel, B., Jalali, M.,
857 and Amann, F.: Hydraulic fracture propagation in a heterogeneous stress field in a crystalline
858 rock mass, Solid Earth, 10, 1877–1904, doi:10.5194/se-10-1877-2019, URL https://www.solid-
859 earth.net/10/1877/2019/, 2019.

860 Feng, X.-T., Young, R., Reyes-Montes, J., Aydan, Ö., Ishida, T., Liu, J.-P., and Liu, H.-J.:
861 ISRM suggested method for in situ acoustic emission monitoring of the fracturing process in rock
862 masses, Rock Mechanics and Rock Engineering, 52, 1395–1414, 2019.

863 Gao, K., Huang, L., Knox, H., Schwering, P. C., Hoots, C., Ajo-Franklin, J., and Kneafsey, T.:
864 Anisotropic Elastic Properties of the First EGS Collab Testbed Revealed from the Campaign
865 Cross-Borehole Seismic Data, in: 54nd US Rock Mechanics/Geomechanics Symposium,
866 American Rock Mechanics Association, 2020.

867 Giese, R. and Jaksch, K.: GFZ Underground Laboratory in the Research and Education Mine
868 "Reiche Zeche" Freiberg, Journal of large-scale research facilities JLSRF, 2, 68, URL
869 http://dx.doi.org/10.17815/jlsrf-2-131, 2016.

870 Gischig, V., Hertrich, M., Krietsch, H., Villiger, L., Doetsch, J., Ma, X., and Doonechaly, N.:
871 Hydraulic Stimulation and Fluid Circulation Experiments in Underground Laboratories: Stepping

872   up the Scale towards Engineered Geothermal Systems, Geomechanics for Energy and
873   Environment, p. 100175, doi:https://doi.org/10.1016/j.gete.2019.100175, 2019.

874   Gischig, V. S., Doetsch, J., Maurer, H., Krietsch, H., Amann, F., Evans, K. F., Nejati, M.,
875   Jalali, M., Valley, B., Obermann, A. C., Wiemer, S., and Giardini, D.: On the link between stress
876   field and small-scale hydraulic fracture growth in anisotropic rock derived from microseismicity,
877   Solid Earth, 9, 39–61, doi:10.5194/se-9-39-2018, URL https://www.solid-earth.net/9/39/2018/,
878   2018.

879   Grehl, S., Sastuba, M., Donner, M., Ferber, M., Schreiter, F., Mischo, H., and Jung, B.:
880   Towards virtualization of underground mines using mobile robots–from 3D scans to virtual
881   mines, in: Proceedings of the 23rd International Symposium on Mine Planning & Equipment
882   Selection, Johannesburg, South Africa, vol. 9, 2015.

883   Guglielmi, Y., Cappa, F., Avouac, J.-P., Henry, P., and Elsworth, D.: Seismicity triggered by
884   fluid injection–induced aseismic slip, Science, 348, 1224–1226, 2015.

885   Haimson, B. and Cornet, F.: ISRM suggested methods for rock stress estimation—part 3:
886   hydraulic fracturing (HF) and/or hydraulic testing of pre-existing fractures (HTPF), International
887   Journal of Rock Mechanics and Mining Sciences, 40, 1011–1020, 2003.

888   Kneafsey, T. and the EGS Collab Team: The EGS Collab Project: An intermediate-scale field
889   test to address enhanced geothermal system challenges, E3S Web Conf., 205, 01 002,
890   doi:10.1051/e3sconf/202020501002, URL https://doi.org/10.1051/e3sconf/202020501002, 2020.

891   Kneafsey, T. J., Dobson, P., Blankenship, D., Morris, J., Knox, H., Schwering, P., White, M.,
892   Doe, T., Roggenthen, W., Mattson, E., et al.: An overview of the EGS Collab project: field
893   validation of coupled process modeling of fracturing and fluid flow at the Sanford Underground
894   Research Facility, Lead, SD, in: 43rd Workshop on Geothermal Reservoir Engineering, Stanford
895   University, paper SGP-TR-213. Preprint at, https://pangea. stanford.
896   edu/ERE/pdf/IGAstandard/SGW/2018/Kneafsey.pdf, 2018.

897   Kneafsey, T. J., Blankenship, D., Knox, H. A., Johnson, T. C., Ajo-Franklin, J. B., Schwering,
898   P. C., Dobson, P. F., Morris, J. P., White, M. D., Podgorney, R., et al.: EGS Collab project:
899   Status and progress, in: Proceedings 44th Workshop on Geothermal Reservoir Engineering,
900   Stanford University, 2019.

901   Krauß, F., Giese, R., Alexandrakis, C., and Buske, S.: Seismic travel-time and attenuation
902   tomography to characterize the excavation damaged zone and the surrounding rock mass of a
903   newly excavated ramp and chamber, International Journal of Rock Mechanics and Mining
904   Sciences, 70, 524–532, 2014.

905   Krietsch, H., Gischig, V., Evans, K., Doetsch, J., Dutler, N. O., Valley, B., and Amann, F.:
906   Stress measurements for an in situ stimulation experiment in crystalline rock: integration of
907   induced seismicity, stress relief and hydraulic methods, Rock Mechanics and Rock Engineering,
908   52, 517–542, 2019.

909 Küperkoch, L., Meier, T., Lee, J., Friederich, W., and Group, E. W.: Automated determination of
910 P-phase arrival times at regional and local distances using higher order statistics, Geophysical
911 Journal International, 181, 1159–1170, 2010.

912 Kwiatek, G., Plenkers, K., and Dresen, G.: Source Parameters of Picoseismicity Recorded at
913 Mponeng Deep Gold Mine, South Africa: Implications for Scaling Relations, Bulletin of the
914 Seismological Society of America, 101, 2592–2608, doi:10.1785/0120110094, 0009 Paper
915 (BSSA), 2011.

916 Kwiatek, G., Martínez-Garzón, P., Plenkers, K., Leonhardt, M., Zang, A., von Specht, S.,
917 Dresen, G., and Bohnhoff, M.: Insights Into Complex Subdecimeter Fracturing Processes
918 Occurring During a Water Injection Experiment at Depth in Äspö Hard Rock Laboratory,
919 Sweden, Journal of Geophysical Research: Solid Earth, 123, 6616–6635,
920 doi:10.1029/2017JB014715, URL
921 https://agupubs.onlinelibrary.wiley.com/doi/abs/10.1029/2017JB014715, 2018 .

922 Manthei, G., Eisenblätter, J., and Dahm, T.: Moment tensor evaluation of acoustic emission
923 sources in salt rock, Construction and Building Materials, 15, 297–309, 2001.

924 Manthei, G. and Plenkers, K.: Review on in situ acoustic emission monitoring in the context of
925 structural health monitoring in mines, Applied Sciences, 8, 1595, 2018.

926 Masuda, K., Nishizawa, O., Kusunose, K., and Satoh, T.: Laboratory study of effects of in situ
927 stress state and strength on fluid-induced seismicity, in: International journal of rock mechanics
928 and mining sciences, Geomechanics abstracts, vol. 30, pp. 1–10, Elsevier, 1993.

929 Mendecki, A., Van Aswegen, G., and Mountfort, P.: A guide to routine seismic monitoring in
930 mines, A handbook on rock engineering practice for tabular hard rock mines, p. 35, 1999.

931 Mjakischew: Untersuchung des Gebirgsspannungszustandes im Südostteil der DDR, in:
932 Freiberger Forschungshefte A740, Beiträge zur Gebirgsmechanik, p. xxx, VEB Deutscher Verlag
933 für Grundstoffindustrie, Leipzig, Germany, 1987.

934 Moore, J., McLennan, J., Allis, R., Pankow, K., Simmons, S., Podgorney, R., Wannamaker, P.,
935 Bartley, J., Jones, C., and Rickard, W.: The Utah Frontier Observatory for Research in
936 Geothermal Energy (FORGE): An International Laboratory for Enhanced Geothermal System
937 Technology Development, in: Proceedings of the 44th Workshop on Geothermal Reservoir
938 Engineering, Stanford University, Stanford, California, 2019.

939 Ohtsu, M.: Simplified moment tensor analysis and unified decomposition of acoustic emission
940 source: application to in situ hydrofracturing test, Journal of Geophysical Research: Solid Earth,
941 96, 6211–6221, 1991.

942 Oldenburg, C., Dobson, P., Wu, Y., Cook, P., Kneafsey, T., Nakagawa, S., Ulrich, C., Siler, D.,
943 Guglielmi, Y., Ajo-Franklin, J., et al.: Intermediate-scale hydraulic fracturing in a deep mine-
944 kISMET project summary 2016, Tech. rep., Lawrence Berkeley National Lab.(LBNL), Berkeley,
945 CA (United States), 2016.

946   Plenkers, K., Kwiatek, G., Nakatani, M., Dresen, G., and Group, J.: Observation of seismic
947   events with frequencies f>25 kHz at Mponeng Deep Gold Mine, South Africa, Seismological
948   Research Letters, 81, 467–478, doi:10.1785/gssrl.81.3.467, 0005 Paper (SRL), 2010.

949   Plenkers, K., Ritter, J. R., and Schindler, M.: Low signal-to-noise event detection based on
950   waveform stacking and cross-correlation: Application to a stimulation experiment, Journal of
951   seismology, 17, 27–49, 2013.

952   Plenkers, K., Schorlemmer, D., Kwiatek, G., and Group, J. R.: On the probability of detecting
953   picoseismicity, Bulletin of the Seismological Society of America, 101, 2579–2591, 2011.

954   Renner, J. and STIMTEC-Team: STIMTEC – A mine-scale hydraulic stimulation experiment
955   of anisotropic metamorphic rock with evaluation by mine-back drilling, in: Introduction to the
956   Special Issue: Deep Underground Laboratories (DUL), edited by Ma, X., vol. Winter 2021, pp.
957   2–4, ARMA Publications Committee, 2021.

958   Rummel, F.: Fracture mechanics approach to hydraulic fracturing stress measurements,
959   Fracture mechanics of rock, p. 217, 1987.

960   Schoenball, M., Ajo-Franklin, J. B., Blankenship, D., Chai, C., Chakravarty, A., Dobson, P.,
961   Hopp, C., Kneafsey, T., Knox, H. A., Maceira, M., et al.: Creation of a mixed-mode fracture
962   network at meso-scale through hydraulic fracturing and shear stimulation, Journal of Geophysical
963   Research: Solid Earth, p. e2020JB019807, 2020.

964   Schopper, F., Doetsch, J., Villiger, L., Krietsch, H., Gischig, V. S., Jalali, M., Amann, F.,
965   Dutler, N., and Maurer, H.: On the variability of pressure propagation during hydraulic
966   stimulation based on seismic velocity observations, Journal of Geophysical Research: Solid
967   Earth, 125, e2019JB018 801, 2020.

968   Sebastian, U.: Die Geologie des Erzgebirges, Springer, 2013.

969   Seifert, T. and Sandmann, D.: Mineralogy and geochemistry of indium-bearing polymetallic
970   vein-type deposits: Implications for host minerals from the Freiberg district, Eastern Erzgebirge,
971   Germany, Ore Geology Reviews, 28, 1–31, doi:https://doi.org/10.1016/j.oregeorev.2005.04.005,
972   URL https://www.sciencedirect.com/science/article/pii/S0169136805000867, special Issue on
973   Electronic Metals, 2006.

974   Stanchits, S. A., Lockner, D. A., and Ponomarev, A. V.: Anisotropic Changes in P-Wave
975   Velocity and Attenuation during Deformation and Fluid Infiltration of Granite, Bulletin of the
976   Seismological Society of America, 93, 1803–1822, 2003.

977   Thomsen, L.: Weak elastic anisotropy, Geophysics, 51, 1954–1966, 1986.

978   Tichomirowa, M., Berger, H.-J., Koch, E., Belyatski, B., Götze, J., Kempe, U., Nasdala, L., and
979   Schaltegger, U.: Zircon ages of high-grade gneisses in the Eastern Erzgebirge (Central European
980   Variscides)—constraints on origin of the rocks and Precambrian to Ordovician magmatic events
981   in the Variscan foldbelt, Lithos, 56, 303–332, 2001.

982   Valliappan, V., Remmers, J., Barnhoorn, A., and Smeulders, D.: A numerical study on the
983   effect of anisotropy on hydraulic fractures, Rock Mechanics and Rock Engineering, 52, 591–609,
984   2019.

985   Van Der Baan, M., Eaton, D., Dusseault, M., et al.: Microseismic monitoring developments in
986   hydraulic fracture stimulation, in: ISRM International Conference for Effective and Sustainable
987   Hydraulic Fracturing, International Society for Rock Mechanics and Rock Engineering, 2013.

988   Vervoort, A., Min, K.-B., Konietzky, H., Cho, J.-W., Debecker, B., Dinh, Q.-D., Frühwirt, T.,
989   and Tavallali, A.: Failure of transversely isotropic rock under Brazilian test conditions,
990   International Journal of Rock Mechanics and Mining Sciences, 70, 343–352, 2014.

991   Villiger, L., Gischig, S., Doetsch, J., Krietsch, H., Dutler, O., Jalali, M., Valley, B., Selvadurai,
992   P. A., Mignan, A., Plenkers, K., et al.: Influence of reservoir geology on seismic response during
993   decameter-scale hydraulic stimulations in crystalline rock, Solid Earth, 11, 627–655, 2020.

994   Warren, W. E. and Smith, C. W.: In situ stress estimates from hydraulic fracturing and direct
995   observation of crack orientation, Journal of Geophysical Research: Solid Earth, 90, 6829–6839,
996   doi:10.1029/JB090iB08p06829, URL
997   https://agupubs.onlinelibrary.wiley.com/doi/abs/10.1029/JB090iB08p06829, 1985.

998   Wadati, K.: On the travel time of earthquake waves.(Part II), Geophys. Mag., 7, 101–111, 1933.

999   Wollin, C., Bohnhoff, M., Martínez-Garzón, P., Küperkoch, L., and Raub, C.: A unified
1000   earthquake catalogue for the Sea of Marmara Region, Turkey, based on automatized phase
1001   picking and travel-time inversion: Seismotectonic implications, Tectonophysics, 747, 416–444,
1002   2018.

1003   Young, R. P., Hazzard, J. F., and Pettitt, W. S.: Seismic and micromechanical studies of rock
1004   fracture, Geophysical Research Letters, 27, 1767–1770, 2000.

1005   Zang, A., Yoon, J. S., Stephansson, O., and Heidbach, O.: Fatigue hydraulic fracturing by
1006   cyclic reservoir treatment enhances permeability and reduces induced seismicity, Geophysical
1007   Journal International, 195, 1282–1287, 2013.

1008   Zang, A., Stephansson, O., Stenberg, L., Plenkers, K., Specht, S., Milkereit, C., Schill, E.,
1009   Kwiatek, G., Dresen, G., Zimmermann, G., et al.: Hydraulic fracture monitoring in hard rock at
1010   410 m depth with an advanced fluid-injection protocol and extensive sensor array, Geophysical
1011   Journal International, 208, 790–813, 2017.
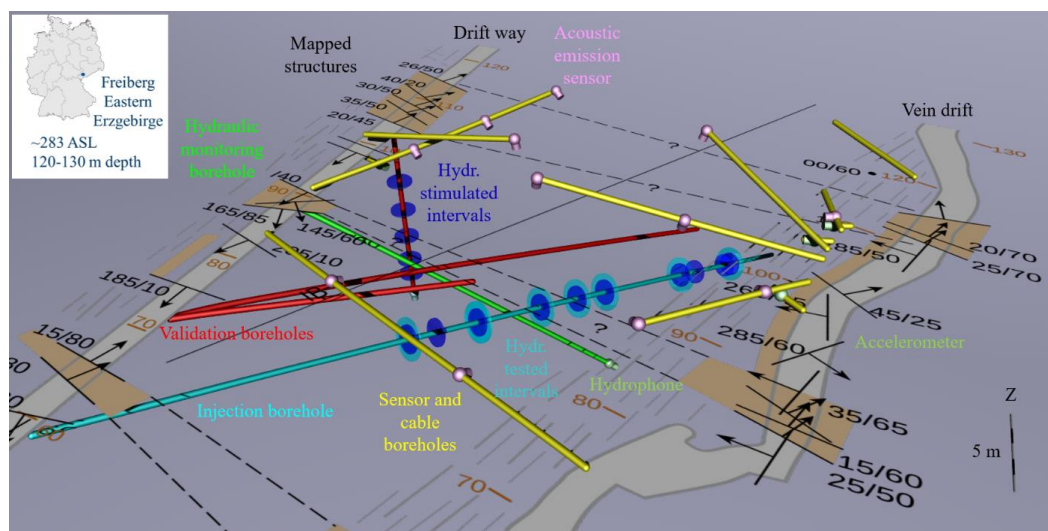
1012

1013

1014

Figure 1: Overview of the borehole network and mapped structures along the galleries at the STIMTEC site in the Reiche Zeche mine. Eastern gallery is the curved vein drift, the western gallery is the straight driftway. Deformation zones (brown zones) marked along the galleries and assumed to belong to connected systems between the galleries based on the orientations of mapped structures identified in the pre-characterisation phase of the experiment are shown. The monitoring system comprises twelve acoustic emission piezo-sensors (purple) located in horizontal or upward going seismic monitoring boreholes (yellow). Three accelerometers (light green) are collocated with AE sensors. A broadband sensor was moved from a short horizontal borehole off the vein drift to the vertical validation borehole (red) in driftway during the course of the experiment. An AE-hydrophone was placed at the bottom of the hydraulic monitoring borehole (green) for the last hydraulic testing phase of the experiment. Stimulation intervals (dark blue) in the injection borehole (cyan) and the vertical validation borehole (red) are shown together with repeatedly tested stimulation intervals (light blue). Inset shows the regional setting of the mine in Freiberg, Germany.

28
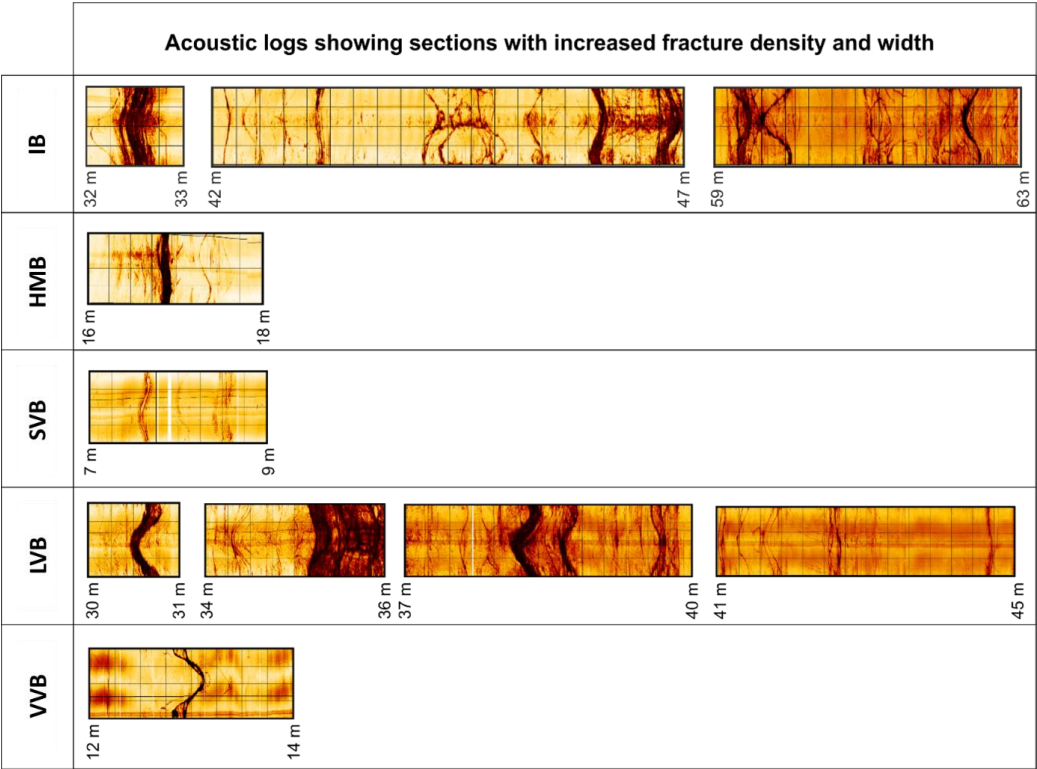
Figure 2: Acoustic borehole televiewer logs indicating sections along the boreholes with increased fracture density and width, intercepted by the injection borehole (IB), hydraulic monitoring borehole (HMB), short inclined (SVB), long inclined (LVB) and vertical (VVB) validation boreholes. Modified from Adero (2020).
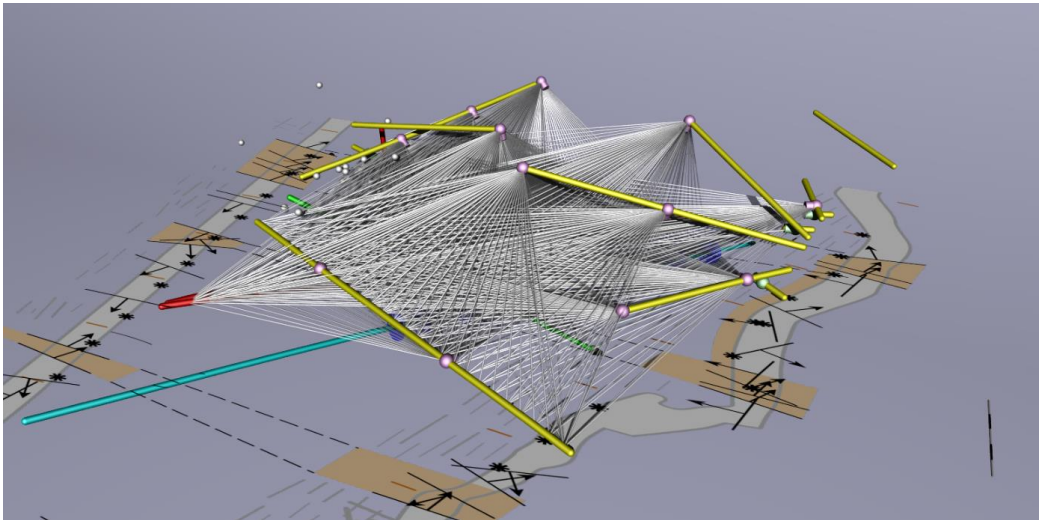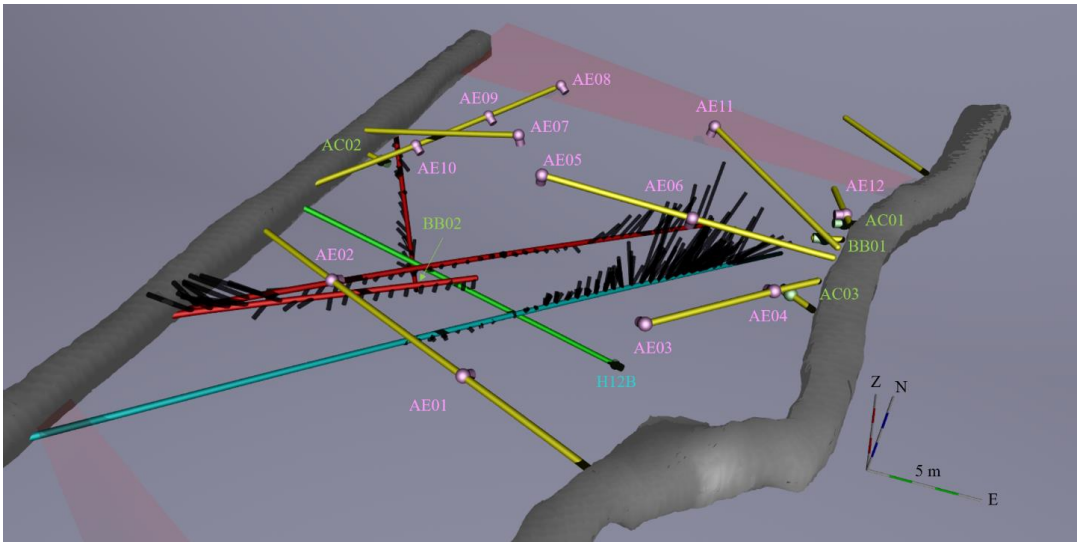

Figure 3: Overview of active seismic measurements within the STIMTEC volume: Ray paths show coverage achieved using UT measurements from boreholes to sensors. Hitpoints (black stars) along the galleries mark positions of repeated active hammer and centre punch measurements.
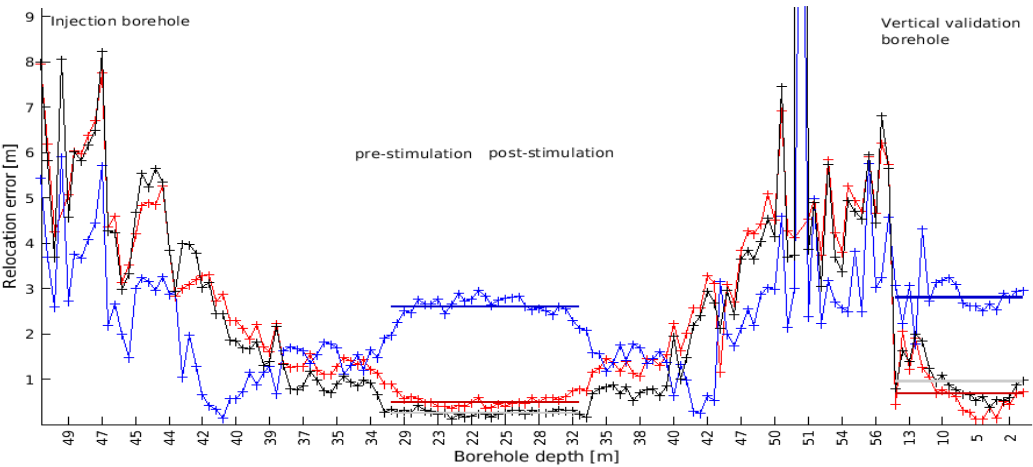
29

1040

1041

1042

Figure 4: a) Overview of location uncertainty estimates (black lines) along the injection and validation borehole as
estimated from locating known UT measurement positions (see Figure 3) with the derived best transverse isotropic
velocity model per seismic sensor. Note that the location error becomes larger than 1 m, where the injection (cyan) and
long inclined validation borehole (red) show higher numbers of fractures and more prominent ones (c.f. Figure 2). Labels
refer to AE sensors (pink), accelerometers or broadband sensor (green, with the broadband sensor being moved to a new
position during the experiment) and AE hydrophone (blue). Deformation zones (pink zones) that transverse the rock
volume between the galleries are shown.

b) Comparison of location error of known active UT measurement points in the injection and vertical validation borehole
for different velocity models. Relocation errors in black are obtained using the best transverse isotropic velocity model per
station, in red from the single transverse isotropic velocity model and in blue from the isotropic velocity model. Coloured
horizontal lines represent averages relocation errors for the given depth range.
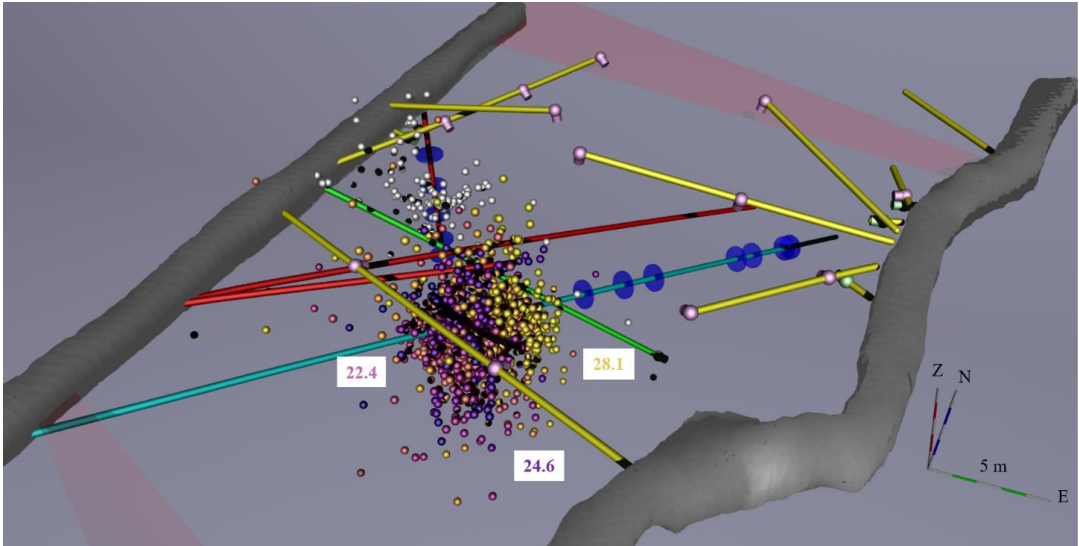
1054

Figure 5: Acoustic emission (AE) locations obtained for stimulation in the injection borehole (coloured dots according to stimulated interval as marked) and the vertical validation borehole (white dots). Note that the intermediate-depth and deep stimulated intervals in the injection borehole produced little to no AE activity
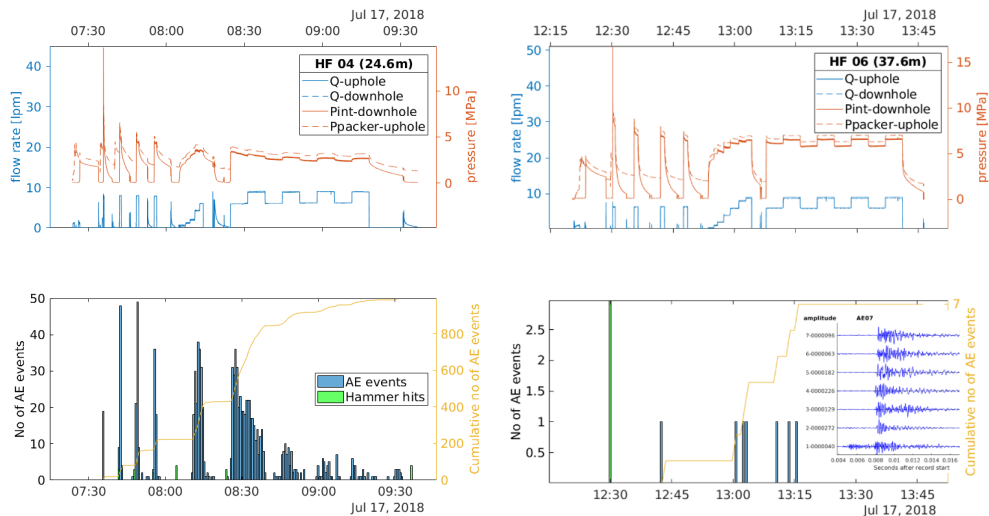

Figure 6: Stimulation sequence consisting of a frac, three refracs, step-rate pump test and periodic pumping test for the intervals at 24.6 m and 37.6 m borehole depth in the injection borehole. Top panel shows flow rate (blue) and pressure records (orange) measured in the intact intervals downhole and at the wellhead uphole, bottom panel shows histogram (blue) and cumulative number (yellow) of located acoustic emission (AE) events. Active hammer hits (green bars) were used as marker signals for the beginning and end of the injection sequence. An example of all the AE events observed during stimulation of interval 37.6 m as recorded by sensor AE07 is shown as an inset.
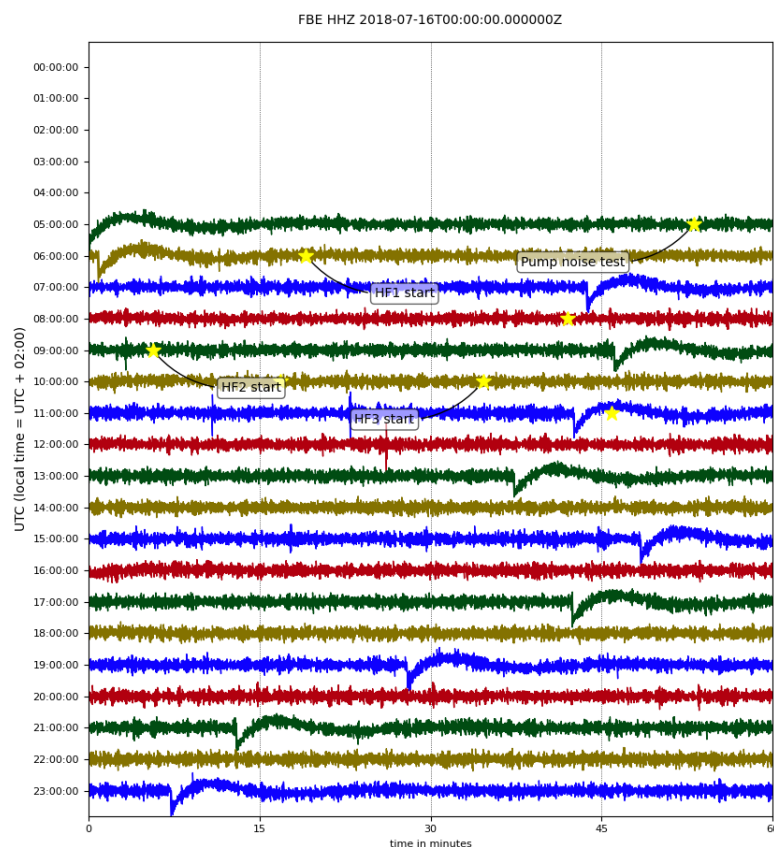
1070
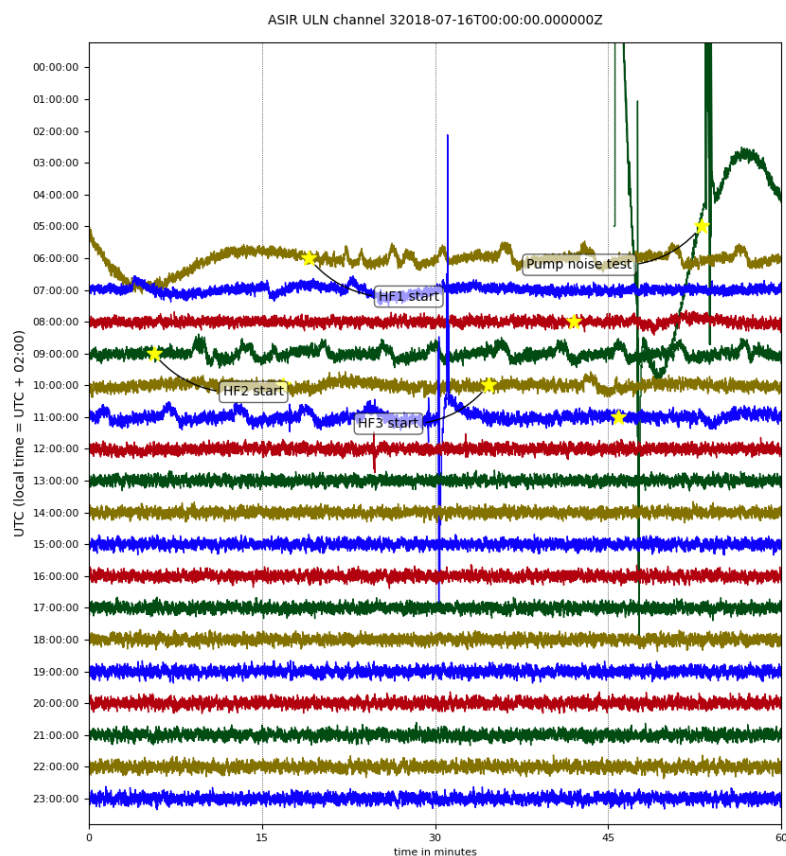
Figure 7: Daily records of the horizontal channel of the ASIR and vertical channel FBE broadband sensor located at Reiche Zeche mine for the first day of stimulation on 16 July 2018. The distance between both sensors is ca. 440 m. Hydrofrac start and end times are marked (by yellow stars and labelled at the start time) as listed in Table 2. Note that long period swings in the records result from bandpass filtering (0.001–1 Hz) in combination with data gaps as seen for the beginning of the records for the ASIR sensor and throughout the day for FBE. Some local quarry blasts are seen on both sensors, whereas stimulation related signals are only visible on the ASIR broadband sensor deployed at the STIMTEC site. Note that the two largest drops seen for the ASIR sensor are likely associated with sensor self-centering as determined on a shake table at GFZ lab after the experiment.
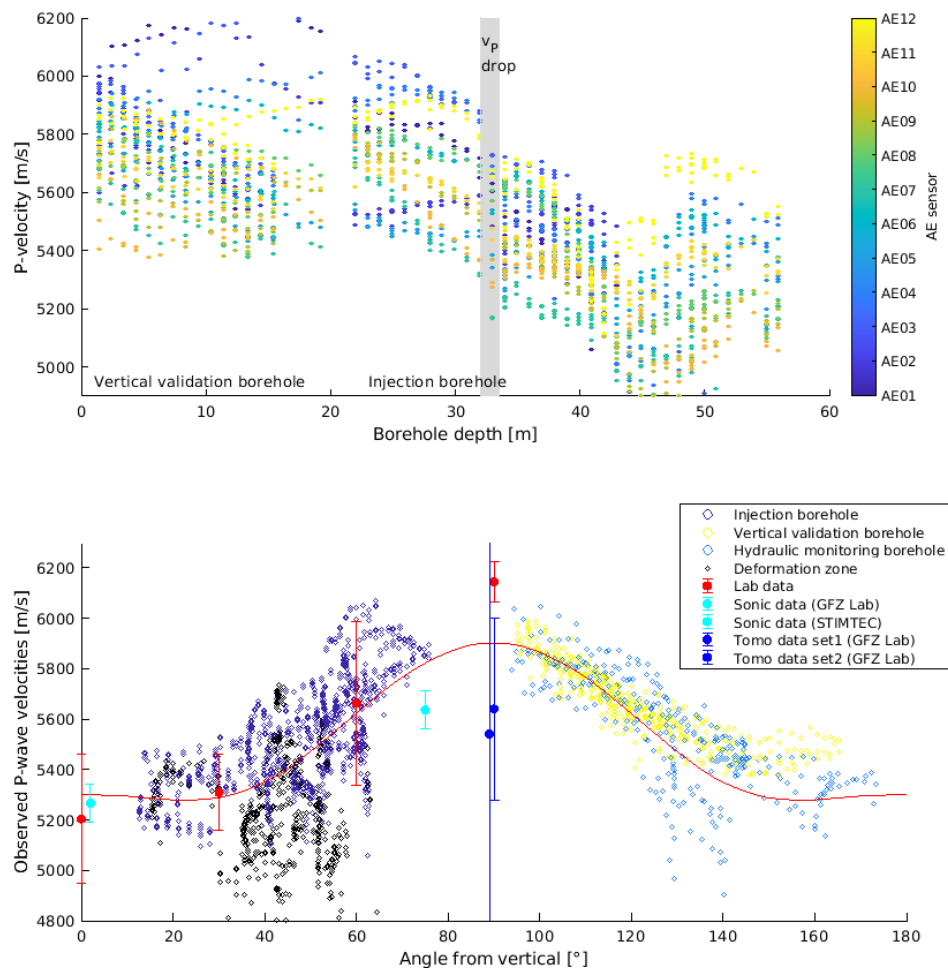
Figure 8: Ultrasonic transmission velocity measurements used for calibration of the transverse isotropic P-wave velocity model shown for measurement depth in the borehole (top) and for angles relative to the vertical symmetry axis (bottom). The red circles display laboratory P-wave measurements (mean and standard deviation) on Freiberg gneiss samples and the red line the theoretical P-wave velocities with incidence angle as determined using the Thomsen parameters derived from the laboratory measurements. Measurement ranges obtained from sonic logs (cyan) from the vertical borehole in the GFZ lab and from the 15°-inclined STIMTEC injection borehole, as well as from P-wave tomography parallel to the foliation direction in the GFZ-lab (blue).

Table 1: Results of stress measurements through overcoring by Mjakischew (1987) at 140 m depth in the Reiche Zeche Mine

Principal stress	Magnitudes [MPa]	Orientation/Plunge [°/°]	
σ1	4.5	347/0	NNW/Horizontal
σ2	3.6	0/90	-/Vertical
σ3	3.0	77/0	ENE/Horizontal

Table 2: Overview of stimulation details for the ten stimulated intervals of the injection borehole. Note that hydraulic characteristics (fracture open/closed injectivity and jacking pressure) were determined from the step rate test. The total injected volume and number of AE events are given for the whole stimulation sequence as shown in Figure 4. The stimulation intervals were chosen to contain as little pre-existing structures as possible based on cores and acoustic logs. The interval condition was reassessed based on the stimulation results as either intact where hydrofracs were created or pre-fractured, meaning that hydroshearing occurred.

Interval	HF10	HF4	HF3	HF5	HF6	HF9	HF8	HF2	HF7	HF1
Depth [m]	22.4	24.6	28.1	33.9	37.6	40.6	49.7	51.6	55.7	56.5
Date (2018)	18/7	17/7	16/7	17/7	17/7	18/7	18/7	16/7	18/7	16/7
Local time start	10:50-	07:20-	12:35-	11:15-	12:20-	09:40-	08:50-	11:05-	07:40-	08:20-
Local time end	12:50	09:35	13:15	12:15	13:45	10:25	09:30	12:15	08:30	10:50
Breakdown p [MPa]	13.3	13.3	11.1	6.4	15.6	9.2	9.4	7.7	5.8	8.2
Injected V [l]	457	466	200	115	327	73	55	145	105	200
mean sensor dist.	19.5	18.7	17.8	17.7	18.5	19.5	24.6	26.0	29.1	29.7
No. AE events	4537	5775	867	6	8	1	0	0	0	0
Pump. period [s]	400	400	90	150	250	–	–	–	100	30–240
Interval condition	intact	intact	intact	frac.	intact	frac.	frac.	frac.	frac.	frac.

Table 3: Minifrac measurement interval details for the vertical validation borehole. See Table 3 for explanation.

Interval	HF15	HF14	HF13	HF12	HF11
Depth [m]	4.0 m	6.7 m	9.3 m	11.7 m	13.2 m
Date (2019)	21/8	21/8	21/8	21/8	20/8
Local time start	11:00-	10:05-	9:00-	8:10-	13:10-
Local time end	11:45	10:46	9:45	8:40	14:00
Breakdown p [MPa]	11.07	14.95	7.95	14.73	7.46
Injected V [l]	22	19	21	18	33
mean sensor dist.	22.5	23.5	24.8	26.1	27.0
No. AE triggers	303	188	52	56	9
Interval condition	frac.	intact	frac.	intact	frac.

Table 4: Parameter setting for automatic picking routine.

parameter	initial pick	final pick
3rd order band-pass filter	[8, 50] kHz	[0.05, 120] kHz
AIC window width	0.0015 s	same?
boundaries for uncertainty limits	[-0.0012, 0.0088] s	
window boundaries for mean energy	[-0.001, 0.009] s	
min SNR (amplitude/standard dev.)	(3,2)	

1110

Table 5: Thomsen parameters (ε, δ, and ɣ) characterising elastic anisotropy of the rock mass derived from fitting all active seismic UT measurements per seismic station. The last two columns give the numbers of measurement points for vP and vS, from which the parameters were derived.

Station	ε	δ	v_{p0}	v_{s0}	γ (fixed)	Number v_p	Number v_s
AE01	0.02	-0.10	5.8	2.9545	0.18	70	58
AE02	0.02	-0.18	5.7	3.2386	0.18	72	36
AE03	0.02	0.14	5.5	2.5568	0.18	63	25
AE04	0.02	0.20	5.9	2.5568	0.18	66	1
AE05	0.08	-0.01	5.4	3.0682	0.18	73	12
AE06	0.16	0.38	5.8	2.6705	0.18	73	6
AE07	0.12	0.14	5.2	2.9545	0.18	73	22
AE08	0.28	0.84	4.6	2.5568	0.18	73	11
AE09	0.14	0.04	5.2	2.8977	0.18	73	49
AE10	0.1	-0.16	5.5	2.6136	0.18	73	32
AE11	0.10	0.26	5.2	2.8977	0.18	73	3
AE12	0.02	-0.22	5.9	2.7841	0.18	71	1
AC02	0.04	-0.18	5.5	3125	0.18	128	0

1115

Table 6: Comparison of root-mean-square residual and number of obtained event locations in the injection (IB) and vertical validation borehole (VVB) obtained using different velocity models. For location accuracy assessment, the average relocation error of the known UT measurement points outside of identified damage zones is provided which represents an average of all values shown in Figure 4b.

1120

36

Velocity model	RMS IB $\cdot 10^{-4}$s (number AE events located with P and S)	RMS VVBH $\cdot 10^{-4}$s (number AE events located with P and S)	Average relocation error outside damage zones (m) (located with P only)
Isotropic model (v_P=5.6 km/s, v_P/v_S=1.76)	2.8± 1.2 (2842)	1.6± 1.3 (401)	1.7±0.80
Transverse isotr. model (v_{P0}=5.3 km/s, v_P0/v_S0=1.76, ϵ = 11.3%)	2.9± 1.3 (3080)	1.3± 1.3 (402)	1.1±0.78
Transverse isotr. model with SNR weighting	1.9± 1.3 (4634)	1.3±1.3 (405)	0.9±0.65
Trans. isotr. model per station (v_{P0}=5.25 km/s, v_P0/v_S0=1.76, ϵ = 12%)	1.6± 1.2 (4613)	1.0± 1.3 (395)	0.8±0.73
Trans. isotr. model per station with SNR weighting	1.5± 1.3 (5531)	0.9±1.3 (392)	0.8±0.70